Separation of Azeotropic Hydrofluorocarbon Refrigerant Mixtures: Thermodynamic and Kinetic Modeling for Binary Adsorption of HFC-32 and HFC-125 on Zeolite 5A

Andrew D. Yancey^{a,b}, Darren P. Broom^c, Mark G. Roper^c, Michael J. Benham^c, David R. Corbin^{a,b}, Mark B. Shiflett^{a,b*}

^aInstitute for Sustainable Engineering, University of Kansas, 1530 W. 15th St., Lawrence, KS 66045, USA

^bDepartment of Chemical and Petroleum Engineering,
University of Kansas, 1536 W. 15th St., Lawrence, KS 66045, USA

^cHiden Isochema Ltd, 422, Europa Boulevard, Warrington, United Kingdom WA5 7TS

*Corresponding Author. Email: Mark.B.Shiflett@ku.edu

Abstract

Hydrofluorocarbons have been used extensively as refrigerants over the past four decades; however, HFCs are currently being phased out due to large global warming potentials. As the next generation of hydrofluoroolefin refrigerants are phased in, action must be taken to responsibly and sustainably deal with the HFCs currently in circulation. Ideally, unused HFCs can be reclaimed and recycled; however, many HFCs in circulation are azeotropic or near-azeotropic mixtures and must be separated before recycling. Previously, pure gas isotherm data were presented for both HFC-125 (pentafluoroethane) and HFC-32 (difluoromethane) with zeolite 5A, and it was concluded that this zeolite could separate refrigerant R-410A (50/50 wt% HFC-125/HFC-32). To further investigate the separation capabilities of zeolite 5A, binary adsorption was measured for the same system using the Integral Mass Balance method. Zeolite 5A showed a selectivity of 9.6 to 10.9 for HFC-32 over the composition range of 25 to 75 mol% HFC-125. Adsorbed phase activity coefficients were calculated from binary adsorption data. The Spreading Pressure Dependent, modified NRTL, and modified Wilson activity coefficient models were fit to experimental data and the resulting activity coefficient models were used in Real Adsorbed Solution Theory (RAST). RAST binary adsorption model predictions were compared with Ideal Adsorbed Solution Theory (IAST) predictions made using the Dual-Site Langmuir, Tóth, and Jensen and Seaton pure gas isotherm models. Both IAST and RAST yielded qualitatively accurate predictions; however, quantitative accuracy was greatly improved using RAST models. Diffusion behavior of HFC-125 and HFC-32 was also investigated by fitting the isothermal Fickian diffusion model to kinetic data. Molecular-level phenomena were investigated to understand both thermodynamic and kinetic behavior.

Introduction

Global climate change has become increasingly relevant as worldwide legislation pushes to mitigate the emission of greenhouse gases (GHGs) including carbon dioxide, methane, nitrous oxide, and fluorocarbons. In 2021, The United Nations (UN) published a report that discussed the current state of the global climate crises and future projections. Among other findings, the report concluded that anthropogenic emission of GHGs led to increased global temperatures resulting in

more sporadic weather patterns including droughts and hurricanes. The report further stressed the importance of mitigating GHG emission to avoid more irreversible damage to Earth.

Fluorocarbons are of particular interest since these chemicals are used in a variety of applications, including air-conditioning, refrigeration, fire suppression, aerosols, and etchants for the semiconductor industry. Chlorofluorocarbons (CFCs) and hydrochlorofluorocarbons (HCFCs) were the first fluorocarbons used as refrigerants starting in the 1930s; however, CFCs were phased out by the Montreal Protocol in 1987, followed by HCFCs in 1992 by the Copenhagen Amendment to the Montreal Protocol, after both were linked to the depletion of the Earth's ozone layer. Hydrofluorocarbons (HFCs) replaced CFCs and HCFCs starting in the mid-1980s, but many HFCs have high global warming potentials (GWPs). A list of commonly used HFCs including GWPs and normal boiling points (NBPs) is provided in the Supporting Information (see Table S1).

Legislation phasing out HFCs has increased in the last two decades and includes the Kyoto Protocol in 2005, F-gas regulations by the European Union in 2014, the Kigali Amendment to the Montreal Protocol in 2016, and the American Innovation and Manufacturing (AIM) act in 2020.² A report published by the National Renewable Energy Lab (NREL) in 2020 estimates that there are currently 2,800 ktons of refrigerant in use globally and that most of this refrigerant consists of HCFCs and HFCs.³ As a result, an increasingly large supply of both HCFC and HFC refrigerant will need to be dealt with as legislation continues to phase them out. Rather than vent or incinerate unused refrigerant, a preferred method is to recycle and reuse these chemicals.

Many of the commonly used HFC refrigerants include azeotropic or near-azeotropic refrigerant blends such as R-507A (50/50 wt% HFC-125/HFC-143a), R-410A (50/50 wt% HFC-32/HFC-125), R-404A (44/52/4 wt% HFC-125/HFC-143a/HFC-134a), and R-407C (23/25/52 wt% HFC-32/HFC-134a). In order to effectively recycle such refrigerants, they must first be separated. In doing so, each species in the mixture can be dealt with individually (e.g., recycled into next-generation refrigerant blends when possible or catalytically converted to high value products or next-generation refrigerants). However, performing such separations to obtain high purity products is difficult because of the similar chemical properties and boiling points of many HFCs and HCFCs. While distillation techniques have been found to be energy-intensive or require the use of entrainers, 4-6 adsorption-based technology is a less energy-intensive process that has been proven to effectively separate both azeotropic and isomeric mixtures. 7-15 Extensive review

articles by Wanigarathna et al. 16 and Yancey et al. 2 discuss fluorocarbon adsorption and separation using adsorbents.

Recently, Wanigarathna et al.^{13, 17} have shown that zeolites 4A, 5A, and 13X are able to separate azeotropic HFC refrigerant mixtures including R-410A, R-404A, R-407C, and R-417A (46.6/50/3.4 wt% HFC-125/HFC-134a/HC-600). Separation of HFC-32 from HFC-125 and from HCFC-22 is shown by the same group using metal-organic frameworks (MOFs).¹² Activated carbons have been used by Sosa et al.⁹ to separate R-410A and R-407F (30/30/40 wt% HFC-32/HFC-134a). Ideal Adsorbed Solution Theory (IAST) was used by Peng et al.⁸ to demonstrate separation of CFC-115 (CFClCF₃) from HFC-125 using Vruf carbon and silicalite. CFC-12 (CF₂Cl₂) and HCFC-22 (CHF₂Cl) are separated by Motkuri et al.⁷ using MOF MIL-101.

Presented is a continuation of a study on using Linde Type A (LTA) zeolites for the separation of R-410A. Our previous work presented pure gas isotherm measurements made for HFC-32 and HFC-125 with zeolites 3A, 4A, and 5A along with enthalpy of adsorption predictions and measurements. It was concluded that both zeolite 4A and 5A have the potential to separate R-410A with the former providing a kinetic separation and the latter a thermodynamic separation. Although zeolite 3A showed potential to kinetically separate R-410A, adsorption of HFC-32 was extremely slow such that its commercial use is not practical.

This work presents experimental binary adsorption data for zeolite 5A with HFC-32 and HFC-125 measured using a Hiden Isochema Intelligent Gravimetric Analyzer (IGA) and XEMIS gravimetric microbalance. The microbalances calculate uptake of each species using the Integral Mass Balance (IMB) method. ¹⁹ In order to design a separation process for R-410A using zeolite 5A, an accurate and reliable thermodynamic model is required. Ideal Adsorbed Solution Theory (IAST) is implemented to predict binary adsorption using pure gas isotherm data from a previous study ¹⁸ and is compared to experimental data. Experimental activity coefficients are calculated, fit to activity coefficient models, and used in Real Adsorbed Solution Theory (RAST) to model binary adsorption of HFC-32 and HFC-125 with zeolite 5A. IAST and RAST models are compared and the accuracy of each model is assessed. Since diffusion rates can affect separation processes, diffusion coefficients are calculated for pure gas adsorption of HFC-125 with zeolite 5A by fitting kinetic data to a Fickian diffusion model.

Models and Methods

Isotherm Equations

Pure gas isotherm models used to describe adsorption of HFC-32 and HFC-125 with zeolite 5A have previously been developed and discussed in detail.¹⁸ A brief description of the relevant equations used in this work is provided.

The Langmuir isotherm model is derived from adsorption kinetics for an energetically homogenous surface. The Dual-Site Langmuir (DSL) model is an extension of the Langmuir model and describes adsorption on energetically heterogenous surfaces. While the Langmuir equation has one term, the DSL equation adds a second, mathematically identical term to represent a total of two energetically different adsorption sites on the adsorbent surface.

$$q(P) = \frac{q_{s1}b_1P}{1+b_1P} + \frac{q_{s2}b_2P}{1+b_2P} \tag{1}$$

where q is the intensive uptake (e.g., mmol/g) of adsorbate on the adsorbent, P is the pressure in the gas phase, q_{s1} and q_{s2} are the saturated uptakes on sites 1 and 2, and b_1 and b_2 are equilibrium parameters for sites 1 and 2. The DSL model includes a total of four fitting parameters, q_{s1} , q_{s2} , b_1 , and b_2 .

Rather than including additional terms, the Tóth isotherm model accounts for the energetic heterogeneity of adsorbent surfaces through a heterogeneity parameter.

$$q(P) = \frac{q_s P}{\left(a_T + P^n\right)^{1/n}} \tag{2}$$

where q_s is the saturated uptake of adsorbate, a_T is the Tóth constant, and n is the heterogeneity parameter, which is constrained to values between 0 and 1. When n is unity, Equation 2 reduces to the Langmuir isotherm. Tóth developed Equation 2 using both theory and experimental measurements.²⁰

Both the DSL and Tóth isotherm models assume that adsorbates do not interact with one another in the adsorbed phase, adsorption occurs on fixed adsorption sites, and the adsorbed phase is immobile and incompressible. Jensen and Seaton²¹ note that at higher pressures, such assumptions

are no longer valid; therefore, this group developed an isotherm model that accounts for the compressibility of the adsorbed phase at higher pressures.

$$q(P) = KP \left\{ 1 + \left[\frac{KP}{a(1 + \kappa_T P)} \right]^c \right\}^{-1/c}$$
(3)

where K is the Henry's law constant, a is a fitting parameter, κ_T is the isothermal compressibility, and c is an empirical fitting constant. When c is unity, Equation 3 reduces to the Langmuir equation; therefore, c describes the degree of heterogeneity of the adsorbent surface. For an incompressible fluid, Equation 3 reduces to the Tóth isotherm. Note that all three isotherm equations (Equations 1-3) predict Henry's law relationship at low pressures and are therefore thermodynamically consistent. Thermodynamic consistency of pure gas isotherm models is required when using the models for multicomponent adsorption predictions.

Ideal Adsorbed Solution Theory (IAST)

Mixture adsorption can be predicted using pure gas isotherm data from each species in the mixture. IAST is a thermodynamic model that predicts multicomponent vapor-adsorption-equilibrium (VAE) data using pure gas adsorption data. The model is based on the thermodynamic requirement of constant chemical potential at VAE and predicts ideal adsorption conditions. The adsorbed phase is considered to be an ideal mixture (IM), whereas the gas phase surrounding the adsorbent is considered to be an ideal gas mixture (IGM). It is also assumed that the amount of adsorbate in the gas phase is constant (i.e., a small amount of adsorbate is adsorbed relative to the amount in the gas phase).

The following expressions for the change in Gibbs free energy are used for the gas phase and the adsorbed phase, respectively.²²

$$dG(P,T,n) = -SdT + VdP + \sum_{i=1}^{N} \mu_i dn_i$$
(4)

$$dG(\pi, T, n) = -SdT + Ad\pi + \sum_{i=1}^{N} \mu_i dn_i$$
 (5)

where G is the Gibbs free energy, S is entropy, V is volume of the gas phase, P is pressure in the gas phase, μ_i is the chemical potential (partial molar Gibbs free energy) of species i, N is the total number of species in the mixture, n_i is the moles of species i in the mixture, A is the surface area of the adsorbent, and π is the spreading pressure in the adsorbed phase (units force/length). The spreading pressure can best be described as a two-dimensional pressure across the surface of the adsorbent and is defined as the negative surface tension.²² The comparison between spreading pressure and surface tension is shown graphically in the Supporting Information (see Figure S1).

Since the surface of an adsorbent is two-dimensional rather than three-dimensional, V and P are replaced by A and π for the adsorbed phase, respectively. Notice that the work terms in Equations 4 and 5 have the same units. A quantitative understanding of the spreading pressure can be elucidated from the expression for changing energy of the adsorbed phase.

$$dU = TdS - \pi dA + \sum_{i=1}^{N} \mu_i dn_i$$
 (6)

where U is the internal energy of the adsorbed phase. From Equation 6, spreading pressure is defined as the following.

$$\pi = -\left(\frac{\partial U}{\partial A}\right)_{S,n} \tag{7}$$

The spreading pressure is a measure of how the internal energy of the adsorbed phase changes with changing surface area. Since the surface area of the adsorbed phase changes during both single and multicomponent adsorption, even when held at constant gas phase pressure and temperature, it is erroneous to assume that the spreading pressure is constant during any adsorption process.

Equations 4 and 5 can be used to derive the expressions for the chemical potentials of the gas phase and the adsorbed phase (full derivation provided in the Supplemental Information). The chemical potentials can be expressed as the following when assuming ideal conditions

$$\mu_i^g \left(T, P, \underline{y} \right) = \mu_i^{o, g} (T) + RT \ln y_i P \tag{8}$$

$$\mu_i^{Ads.}(T,\pi,\underline{x}) = \mu_i^o(T,\pi) + RT \ln x_i \tag{9}$$

where $\mu_i^g\left(T,P,\underline{y}\right)$ is the chemical potential of component i in the gas phase, $\mu_i^{o,g}(T)$ is the chemical potential of species i in the gas phase at the reference state (chosen to be an ideal gas for pure component i), y_i is the gas phase mole fraction of species i, $\mu_i^{Ads.}(T,\pi,\underline{x})$ is the chemical potential of species i in the adsorbed phase, $\mu_i^o(T,\pi)$ is the chemical potential of species i in the adsorbed phase mole fraction of species i, i is the universal gas constant, and i is temperature. At VAE, the chemical potential for each species in the gas and adsorbed phase are equal; therefore, Equations 8 and 9 are set equal, resulting in the following expressions for adsorption of a binary mixture (the complete derivation is provided in the Supplemental Information).

$$x_1 P_1^o(\pi_1) = y_1 P \tag{10}$$

$$x_2 P_2^o(\pi_2) = y_2 P \tag{11}$$

$$\pi_1 = \pi_2 \tag{12}$$

$$x_1 + x_2 = 1 (13)$$

$$y_1 + y_2 = 1 (14)$$

The parameter $P_i^o(\pi_i)$ is the pressure required in the gas phase to reach the spreading pressure for pure component i in the adsorbed phase at VAE.²³ Equations 10 and 11 follow directly from the equifugacity requirement for VAE, whereas Equations 13 and 14 follow from the mass balances for the adsorbed phase and gas phase, respectively. The spreading pressures for all species in the adsorbed phase must be equal at VAE, resulting in Equation 12.²² Equations 10, 11, 13, and 14 are analogous to Raoult's Law for describing ideal behavior at vapor-liquid-equilibrium (VLE). The temperatures of the adsorbed and gas phases are equal at VAE.

When predicting binary VAE data, either the gas phase or adsorbed phase mole fractions of species 1 and 2 are defined, as well as the gas phase pressure. The quantities $P_1^o(\pi_1)$ and $P_2^o(\pi_2)$ are not measurable.²² When the gas phase mole fractions and pressure are defined, this results in four equations (Equations 10-13) for solving VAE conditions with six unknowns: π_1 , π_2 , $P_1^o(\pi_1)$, $P_2^o(\pi_2)$, x_1 , and x_2 .

A fourth equation that would greatly simplify solving for VAE data would relate the spreading pressure in the adsorbed phase for a given species to the gas phase pressure, $f = \pi_i(P)$ (i.e., how much gas phase pressure is required to achieve the spreading pressure for VAE conditions). Expressions for π_1 and π_2 could be substituted into Equation 12, bypassing the need to explicitly solve for π_1 and π_2 . These expressions are derived using the Gibbs-Duhem equation for the adsorbed phase.

$$0 = SdT - Ad\pi + \sum_{i=1}^{N} n_i d\mu_i$$
(15)

When Equation 15 is applied to pure gas adsorption at constant temperature (conditions at which pure gas isotherms are measured), the first term in Equation 15 is zero and the summation is simplified to one term. Since the chemical potential of the adsorbed phase is equal to the chemical potential of the gas phase at VAE, rearranging Equation 15 yields the following set of equations for binary adsorption (the full derivation is provided in the Supplemental Information).

$$\frac{A\pi_1(P_1^o)}{RTm_{Ads.}} = \frac{\Psi_1(P_1^o)}{m_{Ads.}} = \widehat{\Psi}_1(P_1^o) = \int_0^{P_1^o} \frac{q_1(P)}{P} dP$$
 (16)

$$\frac{A\pi_2(P_2^o)}{RTm_{Ads.}} = \frac{\Psi_2(P_2^o)}{m_{Ads.}} = \widehat{\Psi}_2(P_2^o) = \int_0^{P_2^o} \frac{q_2(P)}{P} dP$$
 (17)

where $q_1(P)$ and $q_2(P)$ are the analytical isotherm equations for species 1 and 2 as a function of gas phase pressure, and the integral has been evaluated from $\pi_i(0) = 0$ to $\pi_i(P_i^o) = \pi_i$ so that P_i^o can be known for i = 1 and 2.²³ The parameters Ψ_1 and Ψ_2 are known as the reduced spreading pressures for species 1 and 2, respectively. Note that the reduced spreading pressures have been divided by the dry mass of the adsorbent, $m_{Ads.}$, to obtain the specific reduced spreading pressure, $\widehat{\Psi}_i$. This has been done for unit consistency since isotherm data is typically provided as an intensive quantity (e.g., mol/g or g/g). Following Equation 12, the (specific) reduced spreading pressures are equal at VAE. Equations 16 and 17 are sometimes referred to as the Gibbs Adsorption Isotherms in literature. Note that Equations 16 and 17 directly relate the spreading pressure of pure species 1 and 2 to the gas phase pressure (i.e., the integration can be performed to any pressure).

Substituting Equations 16 and 17 into Equation 12 results in the following expression.

$$\widehat{\Psi}_1(P_1^o) = \int_0^{P_1^o} \frac{q_1(P)}{P} dP = \int_0^{P_2^o} \frac{q_2(P)}{P} dP = \widehat{\Psi}_2(P_2^o)$$
 (18)

Four equations have now been formulated (Equation 10, 11, 13 and 18) that can be used to solve for the four unknowns P_1^0 , P_2^0 , x_1 , and x_2 . Note that when using Equation 18, this avoids needing to solve for π_1 and π_2 explicitly. Also note that Equation 18 requires the use of pure gas adsorption data that can be integrated numerically or analytically.

After the adsorbed phase mole fractions have been solved for at each data point, the total uptake on the adsorbent can be calculated using the following expression.

$$\frac{1}{q_{tot}} = \frac{x_1}{q_1} + \frac{x_2}{q_2} \tag{19}$$

where q_{tot} is the total uptake, and both q_1 and q_2 can be found from pure gas adsorption data (or analytical isotherm expressions) evaluated at the defined mixture pressure. The selectivity can be calculated using the definition for selectivity.

$$S_{1,2} = \frac{x_1/y_1}{x_2/y_2} \tag{20}$$

The full derivation for IAST as well as assumptions made are provided in the Supplemental Information.

Real Adsorbed Solution Theory (RAST)

The IAST model for predicting VAE can be improved if neither the adsorbed nor gas phases are considered ideal. Without the assumption of ideality, Equation 10 is generalized as the following equifugacity expression.

$$x_i \gamma_i (T, \pi, \underline{x}) P_i^o(\pi_1) = y_i P \overline{\varphi}_i^g (T, P, \underline{y})$$
 (21)

The full derivation of Equation 21 is provided in the Supplemental Information. Both the fugacity coefficient for species i in the gas phase, $\overline{\varphi}_i^g(T, P, \underline{y})$, and the activity coefficient for species i in the adsorbed phase, $\gamma_i(T, \pi, \underline{x})$, have been included. Equation 21 is the foundation for Real

Adsorbed Solution Theory (RAST) and is analogous to the γ - ϕ method for solving VLE.²⁴ As noted by Myers and Prausnitz,²² there are many instances in which IAST can be used to sufficiently describe mixture adsorption. Other systems (i.e., those including adsorbates having large dipole moments, adsorbents that are energetically heterogenous, or when the system is at high pressure) can significantly stray from ideality and IAST is not sufficient. Other models that have been used to account for nonidealities in mixture adsorption include Heterogenous Ideal Adsorbed Solution (HIAS) theory,²⁵ Vacancy Solution Theory (VST) employing the Wilson and Flory-Huggins activity coefficient models,²⁶⁻²⁸ and equations of state²⁹ among other more fundamental thermodynamic models and simulations.³⁰⁻³³ RAST has proved to be among the most accurate.

When pressures are not exceedingly large, the fugacity coefficient of the gas phase can be taken as unity; therefore, Equation 21 reduces to the following expressions for binary adsorption.

$$x_1 \gamma_1 \left(T, \Psi, \underline{x} \right) P_1^o(\Psi_1) = y_1 P \tag{22}$$

$$x_2 \gamma_2 \left(T, \Psi, \underline{x} \right) P_2^o \left(\Psi_2 \right) = y_2 P \tag{23}$$

The spreading pressure has been expressed as the reduced spreading pressure in Equations 22 and 23 since this is a more convenient quantity with which to work. The use of Equations 22 and 23 for predicting VAE include an added challenge—an activity coefficient model that sufficiently describes the adsorbed phase must be used. Furthermore, fitting parameters in this activity coefficient model will have either been predicted or obtained from fitting the model to experimentally determined activity coefficients.

For VLE, calculating experimental activity coefficients from equifugacity expressions is straightforward when provided experimental data (i.e., the vapor pressure, a predictable or known property, replaces $P_1^o(\pi_1)$ in Equation 22; therefore, only the activity coefficient is unknown). For VAE, however, $P_1^o(\pi_1)$ and $P_2^o(\pi_2)$ cannot be determined experimentally.

Given experimental mixture adsorption data (i.e., P, x_1 , x_2 , y_1 , y_1 , and total moles adsorbed), six unknowns exist in Equations 22 and 23: $\gamma_1(T, \Psi, \underline{x})$, $\gamma_2(T, \Psi, \underline{x})$, $P_1^o(\Psi_1)$, $P_2^o(\Psi_2)$, Ψ_1 , and Ψ_2 . At present, five equations have been developed that can be used to find the activity coefficients of the adsorbed phase: Equations 16-18, 22, and 23. Equation 18 is always true for binary VAE. The only assumption made when developing Equations 16 and 17 was that the gas phase is ideal. This

same assumption was made in developing Equations 22 and 23; therefore, Equations 16 and 17 are still valid for RAST calculations.

A sixth equation is needed to solve for adsorbed phase activity coefficients and this comes from the Gibbs-Duhem equation for the adsorbed phase (Equation 15), but this time applied to the adsorption of a mixture instead of a pure species as was done previously. When using binary mixture adsorption data at constant temperature and gas phase pressure, Equation 15 reduces to the following (see Supplemental Information for more detail).

$$\frac{Ad\pi}{RT} = d\Psi = \left(\frac{n_1}{y_1} - \frac{n_2}{y_2}\right) dy_1 \tag{24}$$

where n_1 is the moles of species 1 adsorbed from experimental data, n_2 is the moles of species 2 adsorbed from experimental data, and y_1 and y_2 are also from experimental data. Note that Equation 24 does not assume constant (reduced) spreading pressure in the adsorbed phase with changing composition. During mixture adsorption, it is nearly impossible to maintain a constant spreading pressure in the adsorbed phase as a function of the species' mole fractions, and such an assumption is invalid.³⁴

Six equations have now been provided (Equations 16-18 and 22-24) that can be used to find the six unknowns $(\gamma_1, \gamma_2, P_1^o, P_2^o, \Psi_1, \Psi_2)$. The method used to solve for the activity coefficients is as follows:

1. Integrate Equation 24 from $y_1 = 0$ to y_{1m} to find the reduced spreading pressure of the adsorbed phase at a given gas phase composition. This results in the following expression.

$$\Psi_m(y_{1m}) = \int_0^{P_m} \frac{n_2(P)}{P} dP + \int_{y_1=0}^{y_{1m}} \left(\frac{n_1}{y_1} - \frac{n_2}{y_2}\right) dy_1$$
 (25)

where y_{1m} is the gas phase mole fraction of species 1 at a given composition. The first term on the right-hand side of Equation 25 follows directly from Equation 17 and has been evaluated from zero to the pressure of the mixture, P_m rather than P_2^o . This term can be evaluated using either an analytical expression for the uptake of species 2 produced from pure gas isotherm data or by numerically integrating pure gas adsorption data. The second term on the right-hand side of Equation 25 is evaluated by numerically integrating mixture

- adsorption data to the composition of interest at constant pressure. The derivation from Equation 24 to Equation 25 is provided in the Supplementary Material.
- 2. Once Ψ_m is found at y_{1m} using Equation 25, Ψ_1 and Ψ_2 are also known since $\Psi_m = \Psi_1 = \Psi_2$ at VAE (Equation 18). Use Equations 16 and 17 to solve for P_1^o and P_2^o , respectively.
- 3. Use Equations 22 and 23 to solve for γ_1 and γ_2 , respectively
- 4. Repeat steps 1-3 at each experimental data point, integrating from $y_1 = 0$ to the respective y_{1m} each time. This should yield a value for Ψ_m , P_1^o , P_2^o , γ_1 , and γ_2 at each data point within the VAE envelope.
- 5. To check for thermodynamic consistency, evaluate Equation 25 across various data points in the mixture adsorption data set (e.g., integrate from $\Psi(y_1 = 0.25)$ to $\Psi(y_1 = 0.50)$ and ensure the equality in Equation 25 holds).²⁴ This method is valid since the reduced spreading pressure is a state function as shown by Talu and Zwiebel.³⁴

The above process can only be used for calculating activity coefficients within the VAE envelope (i.e., not at zero and one mole fraction of species 1 or 2). Notice that the second term on the right-hand side of Equation 25 involves integrating from $y_1 = 0$. This is problematic since this variable is in the denominator of the integrand. The value for the integrand at $y_1 = 0$ must be estimated by taking the limit of the integrand as $y_1 \to 0$. This method has been used previously by Talu³⁴⁻³⁶ and results in the following expression.

$$\lim_{y_1 \to 0} \left(\frac{n_1}{y_1} - \frac{n_2}{y_2} \right) = n_T \left[\lim_{y_1 \to 0} \left(S_{1,2} \right) - 1 \right]$$
 (26)

The full derivation for Equation 26 is provided in the Supplemental Information. The limit term on the right-hand side of the equality can be found by plotting experimental selectivity values as a function of y_1 and extrapolating the data to the y-intercept. Once the value for the integrand of Equation 25 has been found at $y_1 = 0$ using Equation 26, Equation 25 can be numerically integrated using experimental data, and the spreading pressure of the mixture at a given data point can be found. Note that the value for n_T in Equation 26 is the uptake at $y_1 = 0$ from mixture adsorption data.

While the activity coefficients for γ_1 and γ_2 are both unity at $x_1 = 1$ and $x_2 = 1$, respectively, the values at $x_1 = 0$ and $x_2 = 0$ must be estimated. An expression for the limiting activity coefficient

can be found by rearranging Equation 22 and taking the limit as the adsorbed phase mole fraction of species 1 approaches 0.

$$\lim_{x_1 \to 0} \gamma_1 = P \lim_{x_1 \to 0} \left(\frac{S_{2,1}}{P_1^o} \right) \tag{27}$$

The full derivation of Equation 27 is provided in the Supplemental Information. The value for the limit can be estimated by plotting experimental values for $\frac{S_{2,1}}{P_1^0}$ within the VAE envelope as a function of x_1 and extrapolating to the y-axis. Note that the same value for γ_1 should be obtained when taking the limit as y_1 approaches 0. Likewise, the activity coefficient at $x_2 = 0$ is estimated using the following expression.

$$\lim_{x_2 \to 0} \gamma_2 = P \lim_{x_2 \to 0} \left(\frac{S_{1,2}}{P_2^o} \right) \tag{28}$$

Once the experimental activity coefficients are found, activity coefficient models must be fit to this data before using RAST. The activity coefficient models used in Equations 22 and 23 must be chosen such that they are thermodynamically consistent with VAE. The activity coefficient of species i must approach unity as the adsorbed phase mole fraction of species i approaches 1 and as the (reduced) spreading pressure of the mixture approaches 0.34

$$\lim_{x_i \to 1} \gamma_i \left(T, \Psi, \underline{x} \right) = 1.0 \tag{29}$$

$$\lim_{W \to 0} \gamma_i \left(T, \Psi, \underline{x} \right) = 1.0 \tag{30}$$

Furthermore, the activity coefficient of species *i* must include a (reduced) spreading pressure dependence. Previous groups have shown that some VLE activity coefficient models can be used to predict VAE.³⁷⁻³⁸ Such models, however, are not thermodynamically consistent with VAE because they lack spreading pressure functionality and cannot predict ideal conditions at low pressures.³⁴

Talu introduced the Spreading Pressure Dependent (SPD) activity coefficient model that is specific to VAE.^{34, 36} This model was developed similarly to the development of UNIQUAC for VLE. For binary adsorption, the SPD model is expressed as the following.

$$\ln \gamma_1 = -s_1 \ln \left[\varphi_1 \alpha_{11} + \varphi_2 \alpha_{21} \right] + s_1 - s_1 \left[\frac{\varphi_1 \alpha_{11}}{\varphi_1 \alpha_{11} + \varphi_2 \alpha_{21}} + \frac{\varphi_2 \alpha_{12}}{\varphi_1 \alpha_{12} + \varphi_2 \alpha_{22}} \right]$$
(31)

$$\ln \gamma_2 = -s_2 \ln[\varphi_1 \alpha_{12} + \varphi_2 \alpha_{22}] + s_2 - s_2 \left[\frac{\varphi_1 \alpha_{21}}{\varphi_1 \alpha_{11} + \varphi_2 \alpha_{21}} + \frac{\varphi_2 \alpha_{22}}{\varphi_1 \alpha_{12} + \varphi_2 \alpha_{22}} \right]$$
(32)

$$\varphi_1 = \frac{s_1 x_1}{s_1 x_1 + s_2 x_2} \tag{33}$$

$$\varphi_2 = \frac{s_2 x_2}{s_1 x_1 + s_2 x_2} \tag{34}$$

where s_1 , s_2 , α_{11} , α_{21} , α_{12} , and α_{22} are fitting parameters. The alpha terms are known as the Boltzmann binary energy terms and are temperature dependent. They can be predicted from isosteric heat of adsorption data if not used as fitting parameters. The alpha terms implicitly account for the spreading pressure of the adsorbed phase through a dependence on lateral interaction potentials between species in the adsorbed phase.^{34,36} The parameters s_1 and s_2 are the shape factors and can be estimated from molecular geometry if not used as fitting parameters.³⁶

Valenzuela and Myers provided a means for relating VLE activity coefficient models to VAE activity coefficient models.³⁹

$$G_{Ads}^{ex} = G_{Liq.}^{ex} (1 - \exp\{-B\Psi\})$$
(35)

where G_{Ads}^{ex} is the Gibbs excess mixing property for the adsorbed phase, G_{Liq}^{ex} is the Gibbs excess mixing property for the liquid phase, and B is a fitting parameter. Equation 35 can be used to find the following expression (see Supplemental Information for more detail).

$$\ln \gamma_i^{Liq.} \left(1 - \exp\{-B\Psi\} \right) = \ln \gamma_i^{Ads.} \tag{36}$$

where $\gamma_i^{Liq.}$ is the activity coefficient for the liquid phase, and $\gamma_i^{Ads.}$ is the activity coefficient for the adsorbed phase. Luberti et al.⁴⁰ applied Equation 36 to the van Laar VLE activity coefficient model to better predict adsorption azeotropes. Both the Wilson and non-random two-liquids (NRTL) activity coefficient models can also be used with Equation 36. For VLE, both models account for differences in local compositions in the liquid phase rather than assuming the molecules are interspersed evenly throughout the liquid. The modified Wilson and NRTL models

for VAE are provided in the Supplemental Information. The SPD, modified Wilson, and modified NRTL activity coefficient models will be used in this work.

Once the activity coefficients have been calculated from experimental data, and after appropriate VAE activity coefficient models have been selected and fit to the experimental activity coefficients, these models can be substituted into Equations 22 and 23, and Equations 13, 18, 22, and 23 can be used to predict VAE conditions after defining gas phase pressure and mole fractions. The following information is needed to fully develop a VAE model using RAST (assuming the fugacity coefficient of the gas phase is unity): pure gas isotherm data for each species in the adsorbing mixture, experimental data for the system of interest, and proper activity coefficient models describing the adsorbed phase.

To enhance uptake predictions, activity coefficient models can be used to predict the total moles adsorbed during binary adsorption.

$$\frac{1}{q_{tot}} = \frac{x_1}{q_1} + \frac{x_2}{q_2} + x_1 \left(\frac{\partial \ln \gamma_1}{\partial \Psi}\right)_{T,\underline{x}} + x_2 \left(\frac{\partial \ln \gamma_2}{\partial \Psi}\right)_{T,\underline{x}}$$
(37)

Equation 37 is similar to Equation 19; however, the last two terms have been added and account for nonidealities in the adsorbed phase. Equation 37 is fully developed in the Supplemental Information.

Diffusion

Diffusion coefficients can be calculated by analyzing the kinetic data from gravimetric and volumetric isotherm experiments. Adsorbent particles are often assumed to be spherical; therefore, the one-dimensional form of Fick's second law in spherical coordinates is the basis for deriving the transient profile for mass uptake as a function of time.

$$\frac{\partial c}{\partial t} = \frac{D}{r^2} \frac{\partial}{\partial r} \left(r^2 \frac{\partial c}{\partial r} \right) \tag{38}$$

where c is the concentration of adsorbate in a spherical adsorbent particle, r is the radius of the adsorbent particle, and D is the Fickian diffusion coefficient. During gravimetric analysis, the

adsorbent is held at constant pressure for each data point. For a constant surface concentration, Equation 38 has the following boundary and initial conditions

$$c(r = R) = c_0 \; ; \quad 0 < t < \infty \tag{39}$$

$$\left. \frac{\partial c}{\partial r} \right|_{r=0} = 0 \; ; \; 0 < t < \infty$$
 (40)

$$c(t = 0) = c_i; \quad 0 < r < R$$
 (41)

where R is the radius of the spherical adsorbent particle, c_0 is the constant surface concentration, and c_i is the initial concentration of adsorbate in the spherical adsorbent particle. The first boundary condition states that a constant concentration of adsorbate exists at the surface of the spherical particle; the second boundary condition states that that there is no change in concentration at the center of the sphere and is a result of symmetry; and the initial condition states that at time zero there is a uniform initial concentration of adsorbate in the spherical adsorbent particle. The initial condition follows from the fact that equilibrium has been established at the previous data point.

Crank has provided the solution to Equation 38, which is provided in the Supplemental Information (concentration profile as a function of time and radial position for a spherical adsorbent particle).⁴¹ When the concentration profile is averaged across the radial position, this results in the average concentration as a function of time with the following expression.

$$Z = \frac{M(t)}{M_{\infty}} = 1 - \frac{6}{\pi^2} \sum_{k=1}^{\infty} \frac{1}{k^2} \exp\left\{-\frac{D}{R^2} k^2 \pi^2 t\right\}$$
 (42)

where M(t) is the mass uptake in one adsorbent particle at time t and M_{∞} is the mass uptake in one adsorbent particle at saturation. The term $\frac{D}{R^2}$ is known as the time constant and is frequently reported for diffusion in adsorbents. Since $\frac{M(t)}{M_{\infty}}$ is a ratio, Equation 42 can be directly fit to kinetic data obtained during gravimetric experiments (i.e., Equation 42 is valid for one spherical adsorbent particle as well as 100 spherical adsorbent particles, assuming that adsorbate molecules uniformly diffuse into all adsorbent particles simultaneously). When fitting Equation 42 to kinetic data, the time constant is the fitting parameter. If the particle size of the zeolite sample is known, the diffusion coefficient can be calculated from the time constant.

When using Equation 42 to find the diffusion coefficient, the following is assumed: no external mass transfer limitations exist (i.e., intraparticle diffusion is much slower than diffusion across a film external to the adsorbent particles), the system is isothermal (i.e., the diffusion rate is slow compared to the rate of heat transfer),⁴² and the quantity of gas adsorbed by the adsorbent is much greater than the amount of adsorbate surrounding the adsorbent. In developing Equation 42, it was also assumed that the diffusion coefficient is constant with changing concentration; however, it has been shown that the diffusion coefficient for adsorption is highly concentration dependent.⁴³ The corrected diffusion coefficient can be found using the Darken Equation.⁴³⁻⁴⁴

$$D = D_0 \frac{\mathrm{d} \ln P}{\mathrm{d} \ln q} \tag{43}$$

where D_0 is the corrected diffusion coefficient, D is the Fickian diffusion coefficient found using Equation 42, and q is the uptake of pure species as a function of pressure. Equation 43 assumes an ideal vapor phase and the derivative term is a thermodynamic correction factor. The full derivation for Equation 43 is provided in the Supplemental Information. Note that for Type I isotherms (i.e., Langmuirian), the slope term in Equation 43 is unity for the linear region (i.e., low pressures). Additionally, the corrected diffusion coefficient should approach the value of the self-diffusion coefficient at all pressures.⁴⁴

As molecules diffuse through a zeolite crystal, energetic barriers exist that the molecule must overcome to continue diffusing. ⁴² The unit cell features of zeolite 5A were previously discussed in detail. ¹⁸ Zeolite 5A consists of a three-dimensional channel network. Large alpha cages exist where the channels intersect, and within the alpha cages are eight cations (four Na⁺ and four Ca²⁺). Possible energetic barriers during the diffusion process for both HFC-125 and HFC-32 include adsorption sites (centered around the cations as will be discussed later) and the single 8-ring (S8R) windows that connect the large alpha cages (potential energy barriers associated with steric hinderances). The energy required to overcome these energetic barriers is known as the activated energy for diffusion and can be determined using the following expression.

$$D = D_{\infty} \exp\left\{\frac{-E_A}{RT}\right\} \tag{44}$$

where E_A is the activation energy for diffusion and D_{∞} is the pre-exponential factor. The activation energy for diffusion can be determined by plotting $\ln D$ as a function of inverse temperature (an

Arrhenius plot) and multiplying the slope of the resulting line by the negative universal gas constant.

Binary Adsorption Measurements

Binary adsorption measurements using HFC-32 and HFC-125 were conducted in two separate instruments: Hiden Isochema Intelligent Gravimetric Analyzer (IGA) and Hiden Isochema XEMIS gravimetric microbalance (more specifically, models IGA-003-MC and XEMIS-003-MC). Both instruments are equipped with quadrupole mass spectrometers for gas composition analysis and use the IMB method for determining adsorption uptake of each species in the mixture on the adsorbent. The IMB method is discussed in more detail in the next section. The instruments will be referred to as the IGA+IMB and the XEMIS+IMB.

The IGA+IMB was previously used to measure binary adsorption of the O₂/N₂ system with zeolite 5A and results were validated against literature values by Talu et al.¹⁹ The current study is the first to present adsorption measurements using the XEMIS+IMB with zeolites. The only other study that presents XEMIS+IMB data was recently published by our group and included measurements with ionic liquids and HFC-125/HFC-32. All measurements in the current study were conducted at Hiden Isochema (Warrington, UK). The XEMIS+IMB setup is shown in the Supporting Information (See Figure S2) and is currently installed at the University of Kansas in the Institute for Sustainable Engineering.

Both the IGA+IMB and XEMIS+IMB were operated in dynamic mode at a constant flow rate, pressure, and temperature throughout data collection. For a given experiment, HFC-32 and HFC-125 were supplied from separate gas cylinders and each fed to a separate Brooks Instrument 5800E Series Thermal Mass Flow Control (MFC). Each gas flow passed through a separate pneumatically actuated 4-way, 2-postion VICI valve (NC60/E3 Valco Instruments Corporation Inc.) and were mixed before entering the reactor. The gas mixture was fed through the bottom of the reactor, passed through the sample container, and the effluent was sampled using a Hiden Analytical Dynamic Sampling Mass Spectrometer (DSMS) to determine the outlet feed mole fractions as a function of time. Throughout data collection, a counterflow of helium was fed through the bottom

of the tare side reactor at a constant flow rate of 5 mL/min. to ensure isobaric and stable balance conditions. The balance cabinet was kept at a constant 328.15 K.

The sample and tare reactors contained a mesh stainless steel bucket (ρ = 8025 kg/m³) hung from a stainless-steel wire that was connected to the balance beam. The tare-side bucket contained stainless steel ball bearings (ρ = 7886 kg/m³) as counterweights. Both instruments are equipped with a platinum resistance thermometer (PRT) with an accuracy of ± 0.1 K and a pressure transducer (GE Sensing PDCR 4020/UNIK 5000) with a range of 0-2.0 MPa and an accuracy of $\pm 0.04\%$ of full scale range. The dynamic weighing ranges of the XEMIS+IMB and IGA+IMB microbalances are 0-290 mg and 0-1 g, respectively, with long term balance stabilities of \pm 5 μ g and \pm 1 μ g.

For both the IGA+IMB and XEMIS+IMB, the temperature of the sample reactor was regulated using either a recirculating Grant water bath controlled by an Optima TX150-R5 heater or an external furnace. The IMB+XEMIS uses a cartridge heater inserted into a stainless-steel metal block surrounding the sample reactor. The sample reactor is fixed in position on the microbalance. The Grant water bath for the XEMIS+IMB sits on an elevator so that it can be raised to immerse the sample and tare reactors into the water bath. During pretreatment, the Grant bath is lowered and the cartridge heater is on. During data collection, the Grant bath is raised and the cartridge heater is off. The IGA+IMB contains cooling jackets that are used with the recirculating Grant water bath to regulate temperature during data collection, whereas the external furnace is used to control heating during pretreatment. Further details were provided by Broom et al.¹⁹

Before running an experiment, approximately 1.0 g of zeolite was placed in the stainless-steel mesh sample bucket, which was then placed on the hangdown wire in the sample reactor. The sample reactor was closed and bolted, and a copper gasket was used to ensure a good seal. After sample loading, the counterweight bucket was placed on a stainless-steel hangdown wire in the tare side reactor of the microbalance. The counterweight was appropriately adjusted to ensure that the microbalance did not go out of range during the entirety of the experiment. After adjusting the counterweight, the tare side reactor was sealed with a stainless-steel (XEMIS+IMB) or copper (IGA+IMB) gasket and tightened.

Experiments were conducted by first feeding 100% HFC-32 to the sample reactor and allowing the adsorbent to become saturated. After saturation, HFC-125 was fed into the sample reactor at a

specified mole fraction and the system was allowed to reach equilibrium. This process was repeated for various feed compositions of the HFC-32/HFC-125 mixture and the MFCs were continually adjusted so that a constant flow rate was maintained. By the end of data collection, the zeolite sample was saturated with HFC-125, and HFC-32 had been desorbed.

Integral Mass Balance (IMB) Method

The IMB method for calculating mass uptake of species i by the adsorbent is based on the mass balance for species i within the sample reactor.

$$\frac{dm_i}{dt} = F^{in}\omega_i^{in} - F^{out}\omega_i^{out} \tag{45}$$

where m_i is the mass of species i, F^{in} is the total mass flow rate fed through the sample reactor, F^{out} is the total mass flowrate leaving the sample reactor, ω_i^{in} is mass fraction of species i fed through the sample reactor, and ω_i^{out} is the mass fraction of species i leaving the sample reactor. After combining Equation 45 with the total mass balance on the sample container, integrating the resulting expression from time zero, correcting the balance reading for buoyancy effects, and accounting for the accumulation of species in the fluid phase, this results in the following expression.

$$M_{i}\Delta N_{i}^{Ads} = F^{in} \int_{t=0}^{t} \left(\omega_{i}^{in} - \omega_{i}^{out}\right) dt + \int_{w(t=0)}^{w(t)} \omega_{i}^{out} dw + \frac{PV^{tot}}{ZRT} \int_{\widehat{M}(t=0)}^{\widehat{M}(t)} \omega_{i}^{out} d\widehat{M} - M_{i}\Delta y_{i} \frac{PV^{gas}}{ZRT}$$
(46)

where M_i is the molecular weight of species i, N_i^{Ads} is the moles of species i adsorbed by the adsorbent, w is the weight reading on the microbalance (raw output), P is the pressure, R is the universal gas constant, T is the temperature, Z is the compressibility factor (accounting for nonideality of the gas), V^{tot} is the total internal volume of the sample reactor, \widehat{M} is the average molecular weight of the gas mixture, y_i is the mole fraction of species i in the gas phase, and V^{gas} is the volume of the fluid within the sample reactor (excludes volume of the sample and any components in the reactor such as the sample container and hangdown wires). Equation 46 is used by the HIsorp software to calculate the moles of species i adsorbed by the adsorbent. The full

development of the IMB method was described by Broom et al.¹⁹ and has also been discussed by Baca et al.⁴⁵

XEMIS Gravimetric Microbalance

A separate Hiden Isochema XEMIS gravimetric microbalance was used to measure pure gas adsorption isotherms for HFC-125 and HFC-32 with zeolite 5A. These data were presented and discussed in our previous study. The XEMIS operates in static, as opposed to dynamic, mode and was previously described in detail. 18

During data collection, gas was fed to the instrument at a constant pressure ramp of 50 mbar/min until the desired target pressure was achieved. A constant pressure was then maintained using an admit and exhaust valve working in tandem. Weight data as a function of time was recorded using HIsorp software, and the system was allowed to reach equilibrium. After the weight reading stabilized, more gas was fed into the XEMIS and the process was repeated until the entire isotherm was measured. Isotherms were measured at 298.15 K, 323.15 K, and 348.16 K.

Zeolite Sample

The same zeolite 5A sample used in our previous study was also used for binary adsorption experiments. The zeolite 5A powder (Lot No. 6029610709901) was obtained from the PQ Corporation and has an ideal unit cell composition of $Ca_4Na_4[(SiO_2)_{12}(AlO_2)_{12}]$. The smaple has an average particle size of 3.226 µm (d10 = 0.692 µm, d90 = 6.304 µm) and a skeletal density of 1048 kg/m³. Before data collection, the zeolite sample was pretreated in the XEMIS+IMB or IGA+IMB under vacuum, using a dry turbomolecular pump system with a base vacuum < 10^{-3} Pa, at 350 °C for 12 hours.

Results and Discussion

Mixture Adsorption Data

Mixture adsorption was measured using the IGA+IMB and XEMIS+IMB at 298.15 K, 0.1 MPa, and a total flowrate of 6.25 mL/min and 6.0 mL/min, respectively. The results are shown in Figure 1. Thermodynamic consistency tests were also performed and are shown in Tables S2 and S3.

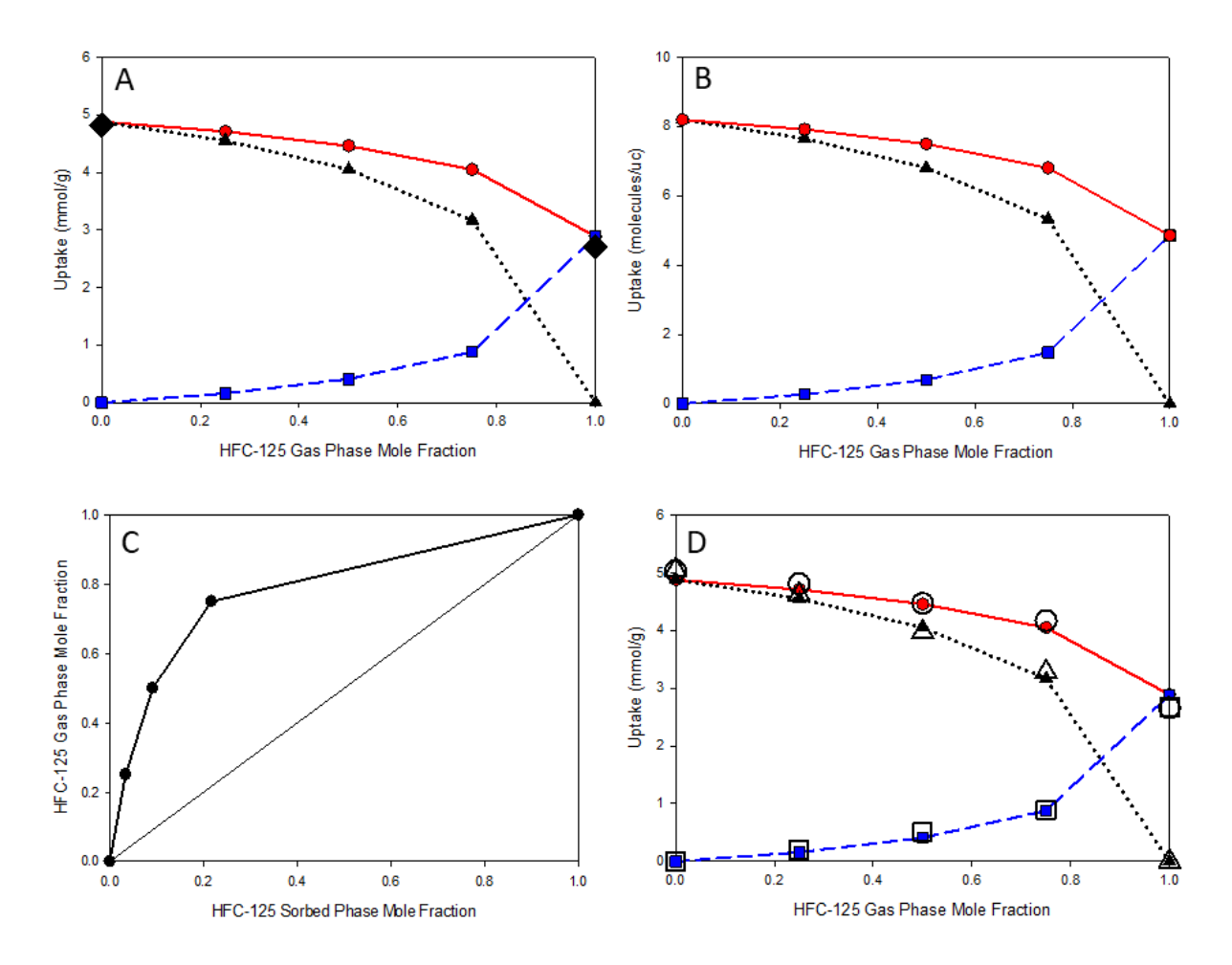


Figure 1. Binary adsorption data for HFC-125 (---■---), HFC-32 (---■---), and total uptake (---■----) on zeolite 5A at 298.15 K, 0.1 MPa, and 6.25 mL/min. in (A) and (D) mmol/g and (B) molecules per unit cell (molecules/uc). (C) x-y diagram for binary adsorption of HFC-125 and HFC-32 on zeolite 5A at 298.15 K and 0.1 MPa. Pure gas adsorption data (•) is plotted in (A) as a comparison. XEMIS+IMB data for HFC-125 (□), HFC-32 (△), and total uptake (○) on zeolite 5A is plotted in (D) and was measured using a flow rate of 6.0 mL/min.

Note that the IGA+IMB data for the final HFC-125 gas phase composition in Figure 1 has been modified for thermodynamic consistency. The data presented at $y_{R125} = 1$ in Figure 1 consists of the following: Total Uptake = 2.89 mmol/g, HFC-125 Uptake = 2.89 mmol/g, HFC-32 Uptake = 0 mmol/g, $x_{R125} = 1.0$, and $x_{R32} = 0$. In reality, the following data were measured: $y_{R125} = 1$, $x_{R125} = 0.924$, $x_{R32} = 0.075$, Total Uptake = 2.89 mmol/g, HFC-125 Uptake = 2.67 mmol/g, HFC-32 Uptake = 0.217 mmol/g. The procedure used for measuring the data consisted of first saturating the adsorbent with HFC-32 followed by simultaneous desorption of HFC-32 and adsorption of HFC-125; therefore, the measured data at $y_{R125} = 1$ likely results from a stronger affinity of zeolite 5A for HFC-32 over HFC-125 as will be discussed below. For thermodynamic consistency, there should be no HFC-32 in the adsorbed phase when there is no HFC-32 present in the gas phase.

Binary adsorption data measured using the IGA+IMB and reported in Figure 1 is consistent with pure gas adsorption data at 0.1 MPa and 298.15 K from our previous study. Pure gas adsorption of HFC-125 and HFC-32 with zeolite 5A was 2.71 mmol/g and 4.82 mmol/g, respectively. Uptake at 1.0 mole fraction HFC-125 reported in Figure 1 is 2.89 mmol/g, whereas uptake reported at 0 mole fraction HFC-125 is 4.88 mmol/g. This is 6.43 % and 1.24 % different than pure gas adsorption results for HFC-125 and HFC-32, respectively. Pure gas adsorption data from our previous study is plotted with binary adsorption data in Figure 1A. Additionally, binary adsorption data measured using the XEMIS+IMB is consistent with IGA+IMB measurements and is shown in Figure 1D. XEMIS+IMB data is provided in the Supplemental Information (see Table S4).

The results in Figure 1 show that zeolite 5A preferentially adsorbed HFC-32 over HFC-125 for most of the gas phase composition range. Furthermore, Figure 1C shows that there will always be a larger mole fraction of HFC-125 in the gas phase than in the adsorbed phase, whereas the opposite is true for HFC-32. Zeolite 5A is an excellent candidate for selectively adsorbing HFC-32 from HFC-125 at any gas phase composition. This behavior is consistent with our previous study, which concluded that zeolite 5A has a larger affinity for HFC-32 over HFC-125.¹⁸

In our previous work, it was proposed that one HFC-32 molecule simultaneously binds to one cation and one framework oxygen atom during pure gas adsorption with zeolite 5A, whereas one HFC-125 molecule binds to two cations and one framework oxygen atom.¹⁸ This suggests that for a given unit cell containing eight cations, theoretically eight HFC-32 molecules should adsorb

(coordinating with eight cations) when zero HFC-125 molecules adsorb. Furthermore, six HFC-32 molecules should adsorb (coordinating with six cations) when one HFC-125 molecule adsorbs (coordinating with two cations), four HFC-32 molecules should adsorb when two HFC-125 molecules adsorb, two HFC-32 molecules should adsorb when three HFC-125 molecules adsorb, and zero HFC-32 molecules should adsorb when four HFC-125 molecules adsorb during coadsorption of the HFCs. These predictions ensure the correct ratio of HFC-125 to HFC-32 molecules for the eight cations per unit cell. The pure component end point trends in Figure 1B are in good agreement with these predictions; however, the mixture results are higher in the number of HFC-32 molecules compared with the prediction.

For example, three HFC-32 molecules adsorbed when three HFC-125 molecules adsorbed, even though two HFC-32 molecules would be predicted. This does not contradict our proposed molecular-level adsorption behavior for each HFC when macroscropic entropic effects are considered. The pure gas isotherms for HFC-32 and HFC-125 with zeolite 5A have been plotted and are provided in the Supporting Information (see Figure S3). using data from our previous work. The regions of enthalpic interactions (adsorption affinity) and entropic interactions (packing efficiency) that control adsorption have been defined as shown in Figure S3.

The binary adsorption experiment shown in Figure 1 was performed at 0.1 MPa. At this pressure, adsorption of both HFC-125 and HFC-32 is entropically driven as shown in Figure S3. As a result, there are more than four HFC-125 molecules per unit cell and more than eight HFC-32 molecules (i.e., there are more molecules of each HFC per unit cell than predicted based solely on ideal enthalpic interactions with eight cations per unit cell). The same phenomenon is expected to occur during binary adsorption at the same pressure (i.e., the predicted number of molecules of each HFC in the adsorbed phase during coadsorption is not expected to perfectly match predictions based on ideal enthalpic interactions). Entropic interactions will affect adsorption behavior at this pressure. Since HFC-32 has a higher packing efficiency than HFC-125 due to smaller molecular size (e.g., kinetic diameter of HFC-32 is 3.9 Å and HFC-125 is 4.4 Å), it is expected that more HFC-32 can adsorb during coadsorption with HFC-125. This is the case when examining Figure 1B (e.g., one HFC-32 molecule adsorbed when four HFC-125 molecules adsorbed instead of zero HFC-32 molecules adsorbing).

Figure 1A shows a low uptake of HFC-125 throughout the gas phase compositions of the HFC mixture until approximately 0.9 gas phase mole fraction of HFC-125. This coadsorption behavior is possibly a result of both enthalpic and entropic considerations during the adsorption process. It was previously concluded that zeolite 5A has a larger affinity for HFC-32 over HFC-125 in part resulting from the larger dipole moment of HFC-32. HEVEN though heats of adsorption from calorimetric measurements were similar (47.35 kJ/mol and 45.72 kJ/mol for HFC-125 and HFC-32, respectively), HEVEN a larger uptake for HFC-32 was observed at lower pressures compared with HFC-125. Additionally, Wanigarathna et al. HEVE-125 broke through at an earlier time than HFC-32 and with a sharper profile. Like zeolite 5A, zeolite 13X is a basic zeolite and is slightly more basic than zeolite 5A based on intermediate Sanderson electronegativity (S_{int}) values (2.56 and 2.38 for zeolites 5A and 13X, respectively). HEVEN ADDITIONAL SHARP AND SHARP

During the coadsorption process, HFC-32 would preferentially fill the high-energy adsorption sites first, whereas HFC-125 would be forced to occupy exclusively low-energy adsorption sites. Here, the high energy adsorption sites refer to simultaneous coordination with cations and framework oxygen atoms, whereas low energy adsorption sites are proposed to be interactions with only the framework oxygen atom. Furthermore, for one HFC-125 molecule to attain an ideal, thermodynamically favored adsorption arrangement as described earlier (i.e., coordinated with two cations and one oxygen atom), the molecule would need to displace two HFC-32 molecules bound more tightly to the intrazeolitic cations. This process is neither enthalpically nor entropically favored considering a species for which the zeolite has lower affinity requires a more specific orientation.

Enthalpically-driven competitive adsorption was noted by Fu et al.⁴⁷ The group showed that FAU zeolites had a larger affinity for HFC-23 (1.65 D) over HCFC-22 (1.46 D) and concluded that HFC-23 competitively fills high-energy adsorption sites, resulting in much lower adsorption of HCFC-22 during coadsorption. The group additionally found that the heat of adsorption for HFC-23 was noticeably larger than HCFC-22, and that both species have similar adsorption arrangement in the adsorbed phase (i.e., simultaneous coordination with one cation and a framework oxygen atom). Molecular level enthalpic interactions were a major factor in the observed competitive adsorption behavior. Since the heats of adsorption for HFC-125 and HFC-32 with zeolite 5A are

similar, it is reasonable to think that the observed competitive adsorption in Figure 1 is influenced by both molecular-level entropic barriers described above in addition to differences in dipole moments.

If adsorption of HFC-125 on high-energy adsorption sites is not favored over HFC-32 for both molecular entropic and enthalpic reasons, there would need to be a larger partial pressure of HFC-125 molecules in the gas phase to overcome these barriers before HFC-125 is the predominant species in the adsorbed phase. This agrees with results in Figure 1, which show that an equimolar composition of the HFCs did not adsorb until a 0.9 gas phase mole fraction of HFC-125. It can be concluded that more HFC-125 would be present in the adsorbed phase during coadsorption if competitive behavior based on both entropic and enthalpic effects were not as prominent.

IAST Predictions

Pure gas adsorption data was provided in our previous study for HFC-125 and HFC-32 with zeolite 5A at 298.15 K. ¹⁸ This data was fit to the DSL, Tóth, and Jensen and Seaton (J-S) isotherm models. The fitting parameters are provided in the Supporting Information (see Table S5) with %AARD for each fit.

The parameters in Table S5 were substituted into Equations 1-3 and the resulting analytical expressions were used when predicting mixture adsorption and performing calculations for both IAST and RAST models. Analytical expressions for the reduced spreading pressure were derived using the Equation 1 for both HFC-32 and HFC-125. Equation 1 was applied to each species, substituted into Equations 16 and 17, and the integrals were solved to yield the following expressions.

$$\frac{A\pi(P_{R125}^o)}{RTm_{Ads.}} = \widehat{\Psi}(P_{R125}^o) = 0.751 \ln(1 + 0.597P_{R125}^o) + 2.70 \ln(1 + 918P_{R125}^o)$$
(47)

$$\frac{A\pi(P_{R32}^o)}{RTm_{Ads.}} = \widehat{\Psi}(P_{R32}^o) = 1.24\ln(1 + 5.69P_{R32}^o) + 4.39\ln(1 + 1055P_{R32}^o) \tag{48}$$

Equations 10, 11, 13, and 18 were used to perform IAST calculations. When implementing the DSL models in IAST, Equations 47 and 48 were directly substituted into Equation 18. This will

be referred to as the IAST-DSL model. When implementing the Tóth and J-S models, the analytical expressions were numerically integrated in Equation 18. Use of the Tóth and J-S models with IAST will be referred to as the IAST-T and IAST-JS models, respectively. IAST predictions were calculated at 0, 0.25, 0.50, 0.75, and 1.0 gas phase mole fractions for HFC-125 at a constant gas phase pressure of 0.1 MPa. Results are provided in Table 1 and Figure 2. The predictions have been plotted against experimental data measured in the IGA+IMB.

Table 1. Results from experimental mixture adsorption and IAST predictions for HFC-32 and HFC-125 with zeolite 5A at 298.15 K and 0.1 MPa.

y_{R125}	<i>x</i> _{R125}	x_{R32}	Total Uptake (mmol/g)	HFC-125 Uptake (mmol/g)	HFC-32 Uptake (mmol/g)	
Experiment	tal Data (IGA	+IMB)	· · · · · · · · · · · · · · · · · · ·	<u> </u>		
0	0	1.00	4.88	0	4.88	
0.25	0.034	0.966	4.71	0.158	4.55	
0.50	0.092	0.908	4.46	0.409	4.05	
0.75	0.217	0.783	4.05	0.878	3.17	
1.0	1.00*	0*	2.89*	2.89*	0*	
DSL Predic	ctions	•	- 1		-	
0	0	1.00	4.80	0	4.80	
0.05	0.003	0.997	4.79	0.013	4.78	
0.15	0.009	0.991	4.77	0.043	4.72	
0.25	0.018	0.982	4.73	0.085	4.65	
0.35	0.030	0.970	4.69	0.141	4.55	
0.45	0.050	0.950	4.69	0.229	4.39	
0.50	0.063	0.937	4.58	0.289	4.29	
0.60	0.100	0.900	4.46	0.446	4.01	
0.75	0.213	0.787	4.12	0.877	3.25	
0.85	0.375	0.625	3.73	1.40	2.33	
0.95	0.709	0.291	3.12	2.21	0.903	
1.0	1.00	0	2.71	2.71	0	
%AARD	15.91	1.06	2.52	16.36	2.39	
Tóth Predic	ctions	•	- 1		-	
0	0	1.00	4.85	0	4.85	
0.05	0.0041	0.996	4.83	0.020	4.81	
0.15	0.015	0.985	4.79	0.070	4.72	
0.25	0.029	0.971	4.74	0.138	4.60	
0.35	0.050	0.950	4.67	0.232	4.44	

0.45	0.080	0.920	4.56	0.363	4.20			
0.50	0.100	0.900	4.50	0.448	4.05			
0.60	0.155	0.845	4.32	0.669	3.65			
0.75	0.303	0.697	3.92	1.19	2.73			
0.85	0.483	0.518	3.52	1.70	1.82			
0.95	0.782	0.218	3.01	2.35	0.655			
1.0	1.00	0	2.72	2.72	0			
%AARD	12.35	2.46	2.24	12.69	3.12			
Jensen and S	Jensen and Seaton Predictions							
0	0	1.00	4.80	0.00	4.80			
0.25	0.027	0.973	4.71	0.128	4.58			
0.35	0.046	0.954	4.69	0.214	4.42			
0.45	0.074	0.927	4.54	0.336	4.21			
0.50	0.093	0.907	4.48	0.416	4.07			
0.60	0.145	0.855	4.32	0.626	3.69			
0.75	0.288	0.712	3.93	1.13	2.80			
0.85	0.466	0.534	3.53	1.65	1.89			
0.95	0.772	0.228	3.01	2.32	0.686			
1.0	1.00	0	2.71	2.71	0			
%AARD	10.65	1.97	2.25	11.22	2.84			

^{*}Data has been modified for thermodynamic consistency of data set. Measurements at this data point consisted of the following: $y_{R125} = 1$, $x_{R125} = 0.924$, $x_{R32} = 0.075$, Total Uptake = 2.89 mmol/g, HFC-125 Uptake = 2.67 mmol/g, HFC-32 Uptake = 0.217 mmol/g.

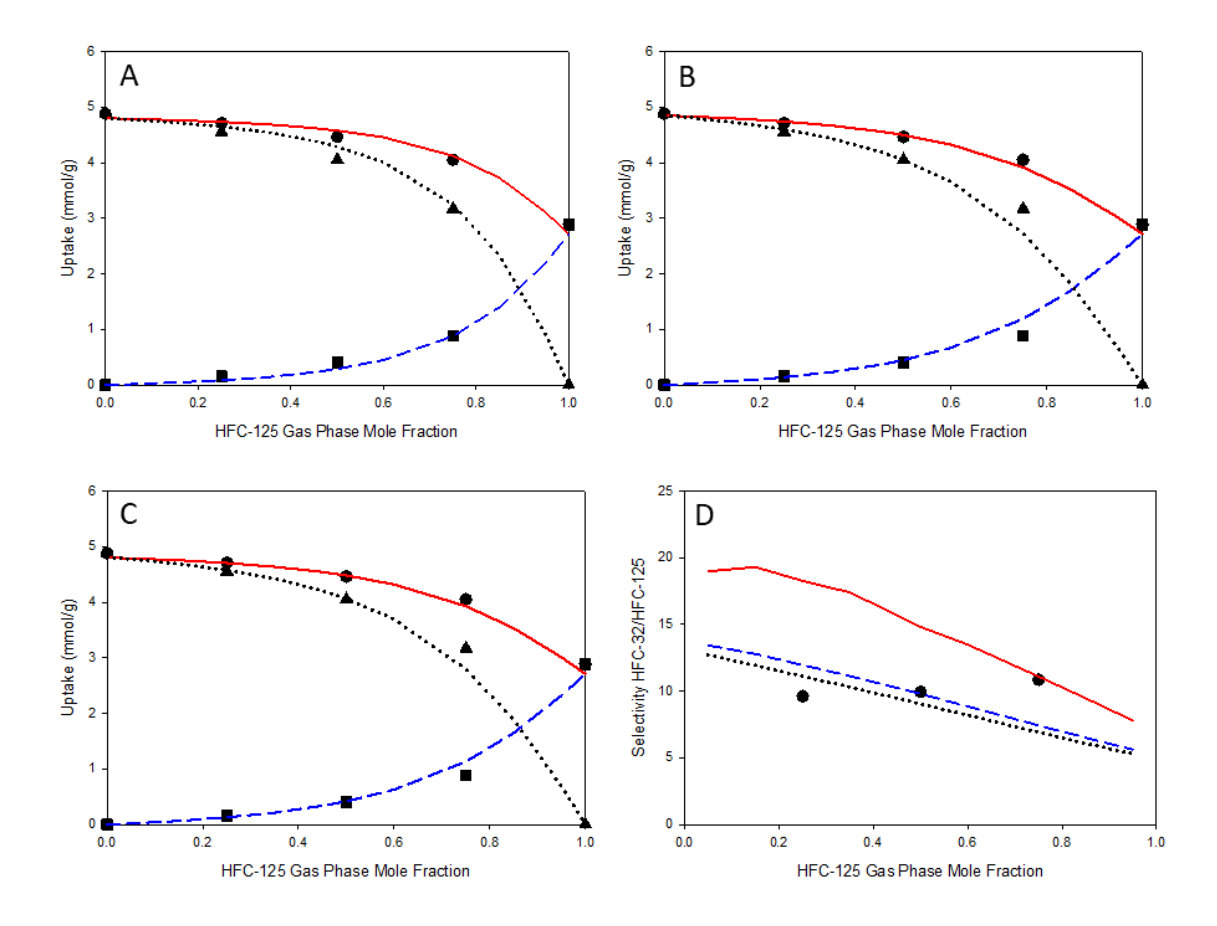


Figure 2. IAST predictions for binary adsorption of HFC-125 (---), HFC-32 (···), and total uptake (—) using the (A) Dual-Site Langmuir (DSL), (B) Tóth, and (C) Jensen and Seaton (J-S) pure gas isotherm models. Predictions are plotted against IGA+IMB experimental data for HFC-125 (■), HFC-32 (▲), and total uptake (•). (D) Selectivity trends from IGA+IMB experimental data (•) and from IAST predictions using DSL (—), Tóth (···), and J-S (---) pure gas isotherm models at 298.15 K and 0.1 MPa.

IAST models provided qualitatively accurate predictions for adsorption of both HFCs. This indicates that coadsorption for HFC-125 and HFC-32 with zeolite 5A is mostly ideal; however, minor qualitative deviations between IAST predictions and reality suggest some degree of nonideality during the adsorption process. A noticeable underprediction of HFC-32 and an overprediction of HFC-125 was observed when using the IAST-T and IAST-JS models at 0.75 gas phase mole fraction of HFC-125. These discrepancies directly affected the point at which an equal

amount of HFC-125 and HFC-32 was adsorbed. This point is shifted slightly to the left for both IAST-T and IAST-JS predictions compared to IAST-DSL predictions.

IAST model predictions were quantitatively less accurate for HFC-125 than for HFC-32 adsorption. This inaccuracy is difficult to see in Figures 2A through 2C since HFC-125 adsorption was small. Although predictions from the IAST-DSL model were slightly closer to experimental results, all IAST models predicted HFC-32 adsorption with similar accuracy (IAST-JS, 2.84 %AARD; IAST-T, 3.12 %AARD; and IAST-DSL 2.39, %AARD). For HFC-125, the IAST-JS model was the most accurate (11.22 %AARD), followed by the IAST-T model (12.69 %AARD). The IAST-DSL model predicted HFC-125 adsorption the least accurately (16.36 %AARD).

Two factors can be attributed to the much larger %AARD values for HFC-125 predictions compared with HFC-32. HFC-125 uptake is small, and combined with the uncertainty of the measurements, small inaccuracies in IAST predictions will yield larger %AARD (i.e., an error of 0.20 mmol/g between experiment and prediction is more significant if the uptake is 0.40 mmol/g compared with 4.0 mmol/g). Additionally, it can be concluded that the nonidealities during coadsorption are associated with HFC-125 adsorption behavior.

Selectivity provides a more sensitive test of the accuracy of binary adsorption equilibria predictions using models,³⁹ and so to further investigate the accuracy of the IAST models, the selectivity for HFC-32 over HFC-125 was predicted by constructing x-y diagrams using the data in Table 1. The selectivity results are provided in the Supporting Information (see Table S6) and the trends are shown in Figure 2D. x-y diagrams are provided in the Supporting Information (see Figure S4).

The predictions for selectivity clearly show differences when using the IAST models with the present system. IAST-DSL predictions led to selectivity values that were 2 to 90% larger than experiment, whereas the IAST-T and IAST-JS models led to more accurate predictions. Interestingly, the most qualitatively accurate model in Figures 2A through 2C yielded the least qualitatively accurate predictions in Figure 2D. This highlights the importance of using models that are both qualitatively and quantitatively accurate. Strikingly, the predicted selectivity trends do not agree with the experimental trends in all cases. The opposite model trends are a direct result of the quantitatively inaccurate predictions for HFC-125 adsorption using IAST.

Note from Figure 2D that IAST predicts a decreasing selectivity trend instead of a constant selectivity throughout the gas phase composition range. Additionally, note that experimental data shows an increasing selectivity. Non-constant selectivity behavior as a function of gas phase composition is characteristic of systems having energetic heterogeneity. As discussed previously, this energetic heterogeneity results from strong electrostatic interactions and hydrogen bonding between the adsorbates having large dipole moments and the zeolite having regions of strong Lewis basicity and acidity. It is interesting that, although IAST predicts the incorrect selectivity trend, the ideal model is still able to capture this energetic heterogeneity.

The inaccuracy of IAST predictions can be explained by examining molecular level adsorption phenomenon. Krishna and Baten⁴⁹ compared molecular simulation results against IAST and RAST predictions for CO₂/N₂, CO₂/CH₄, and CO₂/C₃H₈. In each case, CO₂ was preferentially adsorbed and selectivity trends predicted by IAST were reversed as is the case in Figure 2D. The group noted that IAST is analogous to Raoult's law, which assumes that each species has the same accessibility to adsorption sites (i.e., a homogenous distribution of each species exists within the pores). This implies equal physical accessibility and chemical affinity; therefore, the group hypothesized that nonidealities arose from unequal distribution of species on adsorption sites within the adsorbent pores. This conclusion was supported through the use of molecular simulations, which showed that CO₂ molecules preferentially adsorbed around cations. In addition, the group showed that selectivity trends for the same species on pure silica FAU zeolites (having an absence of cations) could accurately be described by IAST.

Although both HFC-32 and HFC-125 coordinate with the cations in zeolite 5A, it was proposed that HFC-32 competitively fills the high-energy adsorption sites, whereas HFC-125 molecules are forced to fill low-energy adsorption sites during coadsorption. This would in fact result in an unequal distribution of the adsorbed species across adsorption sites. The difference in molecular adsorption arrangement of each species (i.e., HFC-32 coordinates with one cation, whereas HFC-125 coordinates with two), combined with the entropic limitations for HFC-125 during coadsorption could lead to a non-uniform adsorption environment and nonideal adsorption behavior.

RAST Predictions

RAST was investigated to obtain a more accurate and reliable model for binary adsorption of HFC-32 and HFC-125 with zeolite 5A. When performing RAST calculations, only the DSL pure gas isotherm model was used in Equation 18. The DSL model described pure gas adsorption of both HFCs with the greatest accuracy and is simpler than the Tóth and J-S models. Experimental activity coefficients were calculated using experimental data from the IGA+IMB in Table 1, and the results are provided in Table 2.

The SPD, modified Wilson, and modified NRTL activity coefficient models were fit to experimental data, and the results are shown in Table 2. The models are shown graphically in Figure 3 and the fitting parameters for the activity coefficient models are provided in the Supporting Information (see Table S7).

Table 2. Activity coefficients obtained from fitting the SPD, modified Wilson, and modified NRTL activity coefficient models to IGA+IMB experimental data at 298.15 K and 0.1 MPa.

Experimental			Modified Wilson		SPD		Modified NRTL		
x_{R125}	x_{R32}	γ_{R125}	γ_{R32}	γ_{R125}	γ_{R32}	γ_{R125}	γ_{R32}	γ_{R125}	γ_{R32}
0	1	0.386	1.00	0.386	1.00	0.386	1.00	0.386	1.00
0.034	0.966	0.525	1.00	0.525	0.996	0.525	0.995	0.525	0.996
0.092	0.908	0.655	1.00	0.691	0.982	0.696	0.978	0.700	0.981
0.217	0.783	0.937	0.975	0.868	0.954	0.877	0.941	0.886	0.953
1.00*	0*	1.00	0.909	1.00	0.877	1.00	0.856	1.00	0.913
	%AARD			2.58	1.67	2.55	2.52	2.49	1.12

^{*}Data has been modified for thermodynamic consistency. Measurements at this data point consisted of the following: $y_{R125} = 1$, $x_{R125} = 0.924$, $x_{R32} = 0.075$.

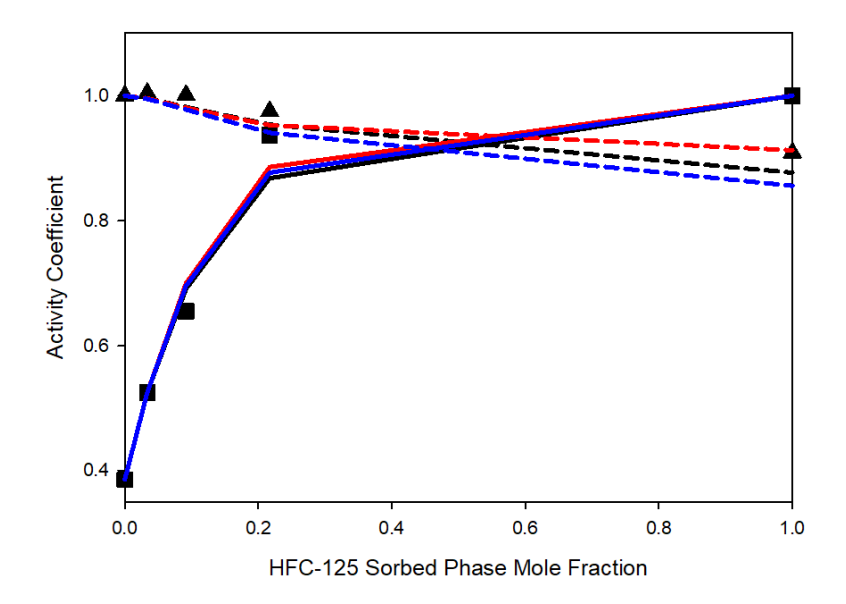


Figure 3. Modified Wilson activity coefficient fits for HFC-32 (---) and HFC-125 (—), modified NRTL activity coefficient model fits for HFC-32 (---) and HFC-125 (—), and SPD activity coefficient model fits for HFC-32 (---) and HFC-125 (—) at 298.15 K and 0.1 MPa plotted against IGA+IMB experimental activity coefficients for HFC-32 (▲) and HFC-125 (■).

The modified NRTL provided a slightly more accurate qualitative and quantitative fit than both the modified Wilson and SPD models. It should be noted that the experimental activity coefficient for HFC-32 at $x_{R125} = 1$ is a rough estimate based on limited data since the largest concentration of adsorbed phase HFC-125 measured was $x_{R125} = 0.217$ as shown in Table 2.

The most striking feature from both Table 2 and Figure 3 is that the experimental activity coefficients for HFC-125 deviate from unity compared with HFC-32 activity coefficients which are closer to unity. A similar phenomenon was reported by Krishna and Baten⁴⁹ when studying CO₂ mixture systems. This group showed that CO₂ was unevenly distributed around cation sites in zeolite 13X during coadsorption with CH₄. As a result, the activity coefficients for CH₄ were less than unity, whereas the activity coefficients for CO₂ were almost always unity over a range of gas phase mole fractions. This was explained based on molecular level pure gas adsorption behavior. Since CO₂ unevenly filled cation sites, this prohibited CH₄ from evenly filling all adsorption sites within the zeolite as it normally would during pure gas adsorption (CH₄ has no

dipole moment). As CO₂ would normally coordinate with cations during pure gas adsorption, molecular level adsorption behavior was not drastically impacted by coadsorption.

The same phenomenon is proposed to occur during coadsorption of HFC-32 and HFC-125. If HFC-32 competitively coordinates with the cations in zeolite 5A during coadsorption, this behavior does not significantly differ from pure gas adsorption. Conversely, if HFC-125 is blocked from the high-energy adsorption sites by HFC-32 during coadsorption, adsorption behavior of HFC-125 differs more during coadsorption than pure gas adsorption; therefore, activity coefficients less than unity are required to correct for this nonideal adsorption behavior.

The slight deviation of HFC-32 activity coefficients from unity results naturally from the increased concentration of HFC-125 in the adsorbed phase. This difference results from adsorbate-adsorbate interactions between HFC-125 and HFC-32, as HFC-125 attempts to fill the high-energy adsorption sites during coadsorption. If HFC-125 molecules are continuously working to overcome both entropic and enthalpic barriers to displace HFC-32 from high-energy adsorption sites, this would affect the adsorption behavior of HFC-32.

Table 2 shows that the activity coefficients for both HFC-125 and HFC-32 are between 0 and 1. Activity coefficients are related to the partial molar Gibbs' excess mixing property of species i through the following relationship.⁵⁰

$$\overline{G}_i^{ex} = RT \ln \gamma_i \tag{49}$$

where \overline{G}_i^{ex} is the Gibbs' partial molar excess mixing property of species i. The Gibbs' molar excess mixing property of species i is the change in Gibbs' excess mixing property with changing moles of species i at constant pressure, temperature, and moles of other species in the mixture. The Gibbs' partial molar excess mixing property of species i is related to Gibbs' free energy change upon mixing through the following relationship.⁵⁰

$$\Delta_{mix}G = \Delta_{mix}G^{IM} + \underline{G}^{ex} = \Delta_{mix}G^{IM} + \sum_{i} x_i \overline{G}_i^{ex}$$
 (50)

where $\Delta_{mix}G$ is the Gibbs' free energy change upon mixing, $\Delta_{mix}G^{IM}$ is the Gibbs' free energy change upon mixing for an ideal mixture, and \underline{G}^{ex} is the total Gibbs' excessing mixing property of the mixture. A negative value for \overline{G}_i^{ex} results in a negative value for $\Delta_{mix}G$, which indicates that

mixing is a favorable process. If values for \overline{G}_i^{ex} are positive, unfavorable interactions have occurred during mixing. The sign of \overline{G}_i^{ex} therefore indicates whether the mixing process is favorable.

For the present case, the term "mixing" refers to the coadsorption of HFC-32 and HFC-125 on the adsorbent. Since the activity coefficients in Table 2 are between 0 and 1, this is related to negative values of \overline{G}_i^{ex} ; therefore, the coadsorption of HFC-125 and HFC-32 on zeolite 5A is a favorable process. This is not surprising since adsorption of HFC-125 and HFC-32 is highly exothermic.

Talu specifically developed the SPD activity coefficient model for adsorption; therefore, fitting parameters from this model can be interpreted with more clarity. The SPD parameters α_{I2} and α_{2I} were defined by Talu.³⁶

$$\alpha_{12} = \exp\left\{-\frac{z(e_{12} - e_{22})}{2RT}\right\} \tag{51}$$

$$\alpha_{21} = \exp\left\{-\frac{z(e_{21} - e_{11})}{2RT}\right\} \tag{52}$$

where e_{ij} is the interaction potential between species i and j in the adsorbed phase and z related to the number of molecules that can coordinate around species i and is positive. Since $\alpha_{12} = 0.746$, this implies that HFC-32 interacting with HFC-125 is less favored than HFC-125 interacting with itself (i.e., e_{12} is larger than e_{22}). Conversely, $\alpha_{21} = 2.05$ indicates that HFC-125 interacting with HFC-32 is more favorable than HFC-32 interacting with itself. The results are consistent with the competitive adsorption behavior between the two HFCs. Since HFC-32 molecules preferentially adsorb to the high-energy binding sites, HFC-32 interactions with HFC-125 would not be favorable. In addition, HFC-32 adsorbate-adsorbate interaction would not be favored since the species would much rather interact with the strong adsorption sites than itself.

The fitting parameters for the modified Wilson and modified NRTL activity coefficient models were originally developed to describe interactions between molecules in a pure liquid state; therefore, elucidating molecular-level phenomenon based on these fitting parameters is not straightforward when applied to VAE. Both adsorbate-adsorbate and adsorbate-adsorbent interactions exist in the adsorbed phase contrary to only adsorbate-adsorbate interactions existing in a pure liquid state. When examining the parameters associated with interaction energy (i.e., Λ_{12}

and A_{21} for the Wilson model, G_{12} and G_{21} for the NRTL model) it is clear that the interaction energy for HFC-125 with HFC-32 is always more negative than those for HFC-32 with HFC-125. The same trend was present with the SPD interaction energy parameters; therefore, it is possible that the physical phenomenon associated with the parameters for the modified NRTL and modified Wilson models can be interpreted in the same manner.

The fitting parameters in Table S7 were substituted into the activity coefficient models, which were used with Equations 13, 18, 22, and 23 to predict VAE at 0.1 MPa and 0, 0.25, 0.50, and 0.75 gas phase mole fractions of HFC-125. Results from RAST predictions are provided in Table 3. Experimental specific reduced spreading pressure, as well as those predicted when using the different activity coefficient models, are presented in Table 3. The values for the reduced spreading pressure at $y_{R125} = 1$ and $y_{R125} = 0$ were calculated using Equations 47 and 48, respectively, in which P_{R125}^o and P_{R32}^o were replaced with mixture conditions (0.1 MPa). Reduced spreading pressures at other data points were found during VAE calculations.

Table 3. VAE predictions using the DSL pure gas adsorption model with the modified Wilson, modified NRTL, and SPD activity coefficient models at 298.15 K and 0.1 MPa.

<i>Y</i> _{R125}	<i>x</i> _{R125}	<i>x</i> _{R32}	γ _{R125}	γ _{R32}	P _{R125} (MPa)	P_{R32}^o (MPa)	$\widehat{\psi}$	
Experimental Data (IGA+IMB) (MPa) (MPa) (mmol/g)								
0	0	1.00	0.386	1.00	-	0.1	21.05	
0.25	0.034	0.966	0.525	1.00	1.418	0.077	19.83	
0.50	0.092	0.908	0.655	1.00	0.834	0.055	18.24	
0.75	0.217	0.783	0.937	0.975	0.369	0.033	15.89	
1.00	1.00*	0*	1.00	0.909	0.100	-	12.28	
Modified Wilson Predictions								
0	0	1.00	-	1.00	-	0.1	21.05	
0.05	0.006	0.994	0.414	1.00	1.97	0.096	20.84	
0.15	0.019	0.981	0.468	0.999	1.70	0.087	20.37	
0.25	0.033	0.967	0.524	0.996	1.43	0.078	19.86	
0.35	0.050	0.950	0.581	0.992	1.20	0.069	19.32	
0.45	0.072	0.928	0.643	0.987	0.979	0.061	18.71	
0.50	0.087	0.913	0.681	0.983	0.847	0.056	18.28	
0.60	0.121	0.879	0.750	0.975	0.659	0.047	17.55	
0.75	0.223	0.777	0.871	0.953	0.387	0.034	16.02	
0.85	0.364	0.636	0.945	0.929	0.247	0.025	14.76	
0.95	0.691	0.309	0.994	0.896	0.138	0.018	13.16	
1.00	1.00	0	1.00	-	0.100	-	12.28	
%AARD	1.78	0.260	2.83	1.22	1.95	1.23	0.261	
Modified N	RTL Predicti	ions			•			
0	0	1.00	-	1.00	-	0.100	21.05	
0.05	0.006	0.994	0.413	1.00	1.97	0.096	20.84	
0.15	0.019	0.981	0.467	0.999	1.70	0.087	20.37	
0.25	0.033	0.967	0.523	0.996	1.43	0.078	19.86	
0.35	0.050	0.950	0.584	0.992	1.19	0.069	19.29	
0.45	0.072	0.928	0.651	0.987	0.957	0.606	18.65	
0.50	0.086	0.914	0.687	0.983	0.849	0.056	18.29	
0.60	0.121	0.879	0.764	0.974	0.647	0.047	17.49	
0.75	0.219	0.781	0.887	0.952	0.385	0.034	16.01	
0.85	0.362	0.638	0.958	0.930	0.245	0.025	14.74	
0.95	0.687	0.313	0.996	0.907	0.139	0.018	13.17	
1.00	1.00	0	1.00	-	0.10	-	12.28	
%AARD	1.71	0.203	2.65	1.26	1.88	1.19	0.252	
SPD Predictions								
0	0	1.00	-	1.00	-	0.100	21.05	

0.05	0.006	0.994	0.413	1.00	1.97	0.096	20.84
0.15	0.019	0.981	0.467	0.998	1.70	0.087	20.37
0.25	0.033	0.967	0.524	0.995	1.44	0.078	19.87
0.35	0.050	0.949	0.583	0.991	1.19	0.069	19.23
0.45	0.072	0.928	0.648	0.984	0.962	0.060	18.66
0.50	0.086	0.914	0.683	0.979	0.852	0.056	18.30
0.60	0.121	0.879	0.757	0.968	0.652	0.047	17.52
0.75	0.223	0.777	0.882	0.939	0.381	0.033	15.98
0.85	0.360	0.643	0.952	0.912	0.250	0.026	14.80
0.95	0.678	0.322	0.995	0.875	0.141	0.018	13.21
1.00	1.00	0	1.00	-	0.100	-	12.28
%AARD	1.99	0.286	2.60	1.68	1.71	1.09	0.228

^{*}Data has been modified for thermodynamic consistency. Measurements at this data point consisted of the following: $y_{R125} = 1$, $x_{R125} = 0.924$, $x_{R32} = 0.075$.

RAST using the DSL pure gas models with the SPD activity coefficient model will be referred to as the RAST-SPD model. Likewise, RAST-W and RAST-N will indicate the use of the DSL pure gas models with the modified Wilson and modified NRTL activity coefficient models, respectively. All RAST models gave similar predictions, with the RAST-N model providing the most accurate predictions.

Predictions for HFC-125 adsorption were more accurate in Table 3 compared with those from IAST in Table 1. Note that HFC-32 predictions in Table 3 are comparable to, or in some instances deviate more from experimental data, than those in Table 1. Although this is the case, it was previously discussed that the main source of non-ideality most likely originates from binary adsorption behavior of HFC-125 rather than from HFC-32. It is therefore expected that RAST predictions would not differ significantly from IAST predictions for HFC-32. The fact that HFC-125 predictions are under 2 %AARD for all model predictions in Table 3 indicates that the activity coefficient models were successful in capturing the nonidealities during coadsorption.

Adsorption phenomenon can be related to the trends and relative values for P_{R125}^o , P_{R32}^o , and $\widehat{\Psi}$ in Table 3. As previously noted, P_i^o is the pressure required in the gas phase to keep pure species i in the adsorbed phase at the spreading pressure for that condition. The data in Table 3 shows that values for P_{R125}^o are generally larger than those for P_{R32}^o . Examining Figures 1B and 1C shows that

one molecule of HFC-125 and six HFC-32 molecules per unit cell are adsorbed at approximately 0.1 adsorbed phase mole fraction of HFC-125. At this point, P_{R125}^o is approximately 0.8 MPa, whereas P_{R32}^o is approximately 0.05 MPa; therefore, a much larger gas phase pressure is required to hold one HFC-125 molecule in the adsorbed phase than to hold six HFC-32 molecules in the adsorbed phase at $\hat{\Psi} = 20.60$ mmol/g. These observations agree with the competitive adsorption phenomenon observed for both HFCs with zeolite 5A. Since the zeolite has a greater affinity for HFC-32, it makes sense that less force (pressure) is required to hold this species in the adsorbed phase at a given constant spreading pressure.

Note from Table 3 that the values for P_{R125}^o and P_{R32}^o decrease as the concentration of HFC-125 increased in both the gas and adsorbed phases. As P_{R125}^o decreased to the gas phase pressure of 0.1 MPa, P_{R32}^o decreases from this pressure. The range of spreading pressures required to establish VAE during coadsorption are easier to attain for pure gas adsorption of HFC-32 than for pure gas adsorption of HFC-125. For example, if HFC-125 was adsorbed onto zeolite 5A until $\hat{\Psi} = 15.89$ mmol/g was attained, this would require 0.369 MPa gas phase pressure, whereas only 0.033 MPa of gas phase HFC-32 pressure would be required to attain the same spreading pressure in the adsorbed phase. The working range of reduced spreading pressures during binary adsorption results from the larger affinity of the zeolite for HFC-32 over HFC-125. This phenomenon was also observed by Costa et al.,³⁷ who reported larger, decreasing P_i^o values for CH₄ relative to those for CH₃CH₃ during coadsorption onto an activated carbon. Pure gas isotherm data showed that the carbon had a larger affinity for CH₃CH₃ over CH₄.

To further investigate the accuracy of the RAST models, data from Table 3 was used to generate an x-y diagram and the selectivity trend as a function of gas phase mole fraction. As noted earlier, selectivity provides a more sensitive test of the accuracy of binary adsorption equilibria predictions. Trends were compared to experimental data and IAST predictions and are shown in Figure 4. Data is presented in the Supporting Information (see Table S8). Only predictions using the RAST-N model are shown in Figure 4 since this was the most accurate model. Similar trends were produced using both the RAST-SPD and RAST-W models and are provided in the Supplemental Information (see Figures S5 and S6). Activity coefficient predictions are additionally provided graphically in the Supporting Information (see Figure S7).

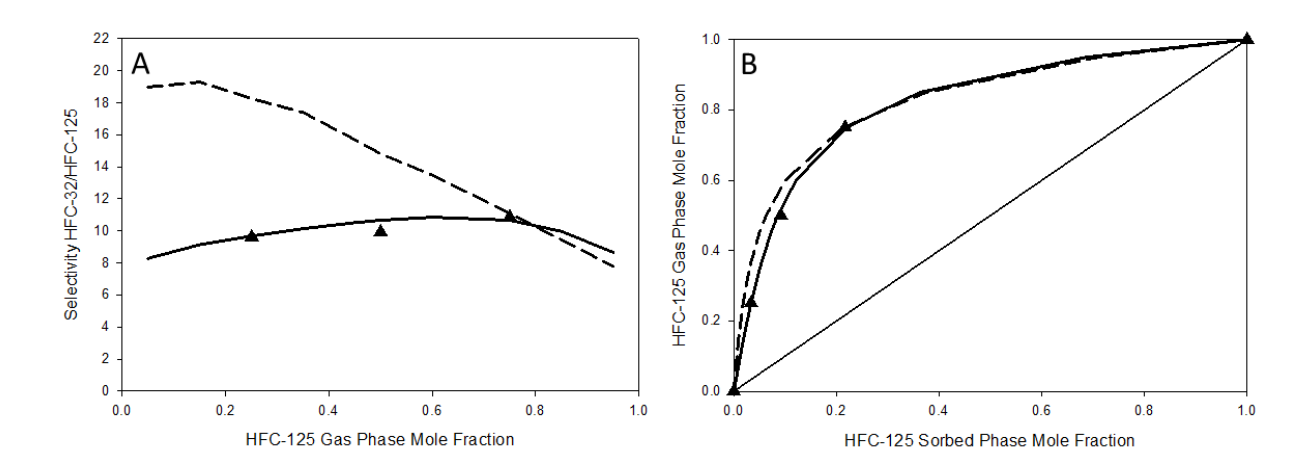


Figure 4. (A) Selectivity for HFC-32 over HFC-125 predicted by the RAST-N model (—) compared to IAST-DSL predictions (---) and (B) x-y diagram predicted by the RAST-N model (—) compared with IAST-DSL predictions (---). Predictions are plotted against IGA+IMB experimental data (▲).

The selectivity trend was greatly improved when adsorbed phase nonidealities were considered using an activity coefficient model. The RAST-N model predicted selectivity with the highest accuracy (3.34 %AARD), followed by the RAST-W (3.48 %AARD) and the RAST-SPD (3.91 %AARD) models. Notice that the selectivity trend generated by the RAST-N model in the experimental range increases instead of decreases as was predicted using IAST. It is interesting that a maximum selectivity is predicted at approximately 0.6 gas phase mole fraction of HFC-125 by the RAST-N model. Throughout the entire gas phase concentration range, the RAST models predicted selectivity values ranging from 8 to 11.

Although the SPD, modified Wilson, and modified NRTL activity coefficient models all contain spreading pressure dependency, only the latter two models explicitly show this dependency and can be used in Equation 37 to calculate total moles adsorbed. Since both models predicted similar adsorbed phase mole fractions, only the modified NRTL model was used with Equation 37 to predict the moles of HFC-125 and HFC-32 adsorbed. Results are shown in Table 4 and Figure 5.

Table 4. Predictions for uptake of HFC-125, HFC-32, and total moles on Zeolite 5A at 298.15 K and 0.1 MPa using the RAST-N model.

<i>y</i> _{R125}	HFC-125 Uptake (mmol/g)	HFC-32 Uptake (mmol/g)	Total Uptake (mmol/g)
0	0	4.80	4.80
0.05	0.030	4.75	4.76
0.15	0.090	4.64	4.73
0.25	0.156	4.52	4.68
0.35	0.233	4.39	4.62
0.45	0.328	4.22	4.55
0.50	0.386	4.12	4.50
0.60	0.533	3.86	4.39
0.75	0.901	3.21	4.11
0.85	1.36	2.39	3.75
0.95	2.16	0.984	3.14
1.0	2.71	0	2.71
%AARD	3.95	1.23	2.14

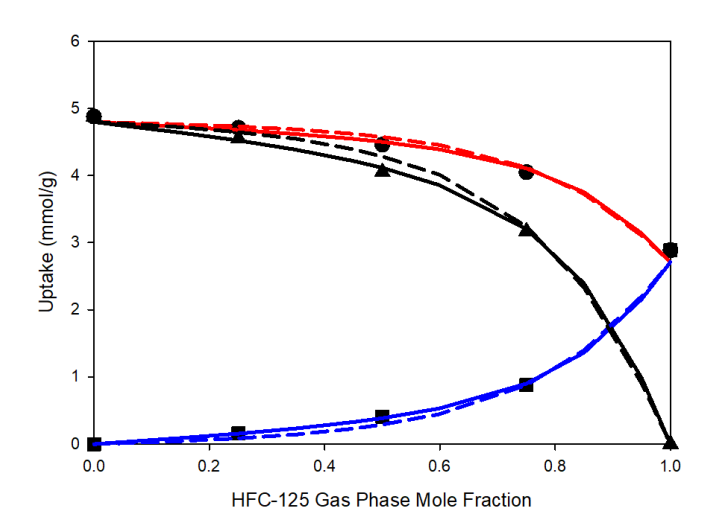


Figure 5. IAST-DSL predictions for HFC-125 (---), HFC-32 (---), and total uptake (---) compared to RAST-N predictions for HFC-125 (—), HFC-32 (—), and total uptake. Predictions are plotted against IGA+IMB experimental data for HFC-32 (▲), HFC-125 (■), and total uptake (•).

Notice from both Figure 4B and Figure 5 that only minor qualitative corrections were made with RAST models relative to IAST-DSL predictions. Figure 5 shows that IAST-DSL slightly overpredicted HFC-32 and slightly underpredicted HFC-125 uptake. Despite small qualitative corrections, the importance of quantitative accuracy is shown in Figure 4A. While the IAST models may provide good qualitative descriptions of coadsorption behavior, it is more appropriate to use RAST models when predicting quantities such as selectivity and for future design of separation processes.

Diffusion Coefficients

Mass versus time data was measured during pure gas adsorption of HFC-125 and HFC-32 from 0 to 1.0 MPa. HFC-32 diffused into zeolite 5A quickly; therefore, Equation 33 could not be appropriately fit to the kinetic data to find diffusion coefficients throughout the pressure range. A ramp rate of 50 mbar/min. was used when changing pressures, and the diffusion rate of HFC-32 into zeolite 5A was faster than the time required to reach the setpoint pressure (i.e., equilibrium uptake was established between HFC-32 and zeolite 5A at all temperatures and pressures by the time the target pressure was reached).

A similar phenomenon occurred with HFC-125 and zeolite 5A in the pressure range of 0.05 MPa to 1.0 MPa. Below a pressure of 0.05 MPa, Equation 42 could appropriately be fit to the constant pressure region of kinetic data using the time constant as the fitting parameter. The diffusion coefficient for HFC-125 with zeolite 5A was calculated using the time constant and the average particle diameter of the zeolite sample. Results are provided in Table 5. When fitting Equation 42 to kinetic data, the summation only required 200 terms. Dimensionless kinetic data (mass versus time) with model fits are provided in the Supplemental Information (Figures S8-S14). The activation energy for diffusion and the pre-exponential factor were also calculated using Equation 44. The Arrhenius plots are provided in the Supplemental Information (Figures S15 and S16).

Table 5. Time constants, diffusion coefficients, activation energy for diffusion, and preexponential factors measured from experimental data at various pressures and temperatures for zeolite 5A and HFC-125.

Pressure (MPa)	Temperature (K)	$\frac{D/R^2}{(1/s)}$	<i>D</i> (m ² /s)	E _A (kJ/mol)	D_{∞} (m ² /s)
1.25 · 10 - 2	298.15	2.97·10 ⁻⁵	7.73 · 10 - 17	43.48	2.95·10 ⁻⁹
	323.15	8.85 · 10 - 5	2.30·10 ⁻¹⁶		
	348.15	3.74 · 10-4	9.73 · 10 - 16		
2.50·10-2	298.15	5.16.10-5	1.34·10 ⁻¹⁶	35.50	2.02·10 ⁻¹⁰
	323.15	1.18 · 10-4	3.07·10 ⁻¹⁶		
	348.15	4.11 · 10 - 4	1.07·10 ⁻¹⁵		
3.75·10-2	298.15	6.46 · 10 - 5	1.68·10-16		

It was assumed that intracrystallite diffusion resistance is the rate-limiting step during the diffusion process in the development of Equation 42 (i.e., diffusion through pores of zeolite crystals and not between zeolite crystals). Since Equation 42 fits the kinetic data at conditions in Table 5 with both good qualitative and quantitative accuracy, this indicates that diffusion of HFC-125 into zeolite 5A was primarily limited by intraparticle resistance (see Figures S8-S14). Furthermore, since the zeolite powder had not been pelletized nor did it include a binder, diffusion rates are representative of micropore diffusion within the zeolite crystals.

The time constants reported in Table 5 are smaller than those obtained by Garcés-Polo et al.⁴² when studying diffusion of CO₂ in zeolite 5A (average of 3.797·10⁻² s⁻¹ at 273 K for values between 0 and 0.1 MPa). This group used a non-isothermal model to obtain the time constant. Additionally, the diffusion coefficients presented in Table 5 at 298.15 K are smaller than that obtained by Sargent and Whitford⁵¹ for CO₂ in zeolite 5A at low pressures (self-diffusion 1.39·10⁻¹⁵ m²/s at 298.15 K). Note that the diffusion coefficients in Table 5 can appropriately be compared with self-diffusion coefficients since pressures are low (i.e., data points are still within the linear region of the adsorption isotherm).⁴³

The results are reasonable considering that HFC-125 (4.4 Å kinetic diameter) is larger than CO₂ (3.3 Å kinetic diameter) and that zeolite 5A has a slightly greater affinity for HFC-125 over CO₂. ^{18,}
⁴² The larger affinity for HFC-125 is observed by comparing the isotherms for each species at low pressures (see Supplemental Information Figure S17). Due to its larger size, HFC-125 should

encounter more steric hinderances than CO₂ when diffusing through zeolite 5A, which would result in slower diffusion. Since zeolite 5A has a larger affinity for HFC-125, this creates additional, stronger energy barriers that HFC-125 must overcome relative to CO₂ diffusion through the zeolite. A decrease in diffusion rate resulting from increased adsorbate-adsorbent interaction was also presented by Carbajo et al.,⁵² who observed a slower diffusion rate for CO₂ in MFI zeolites with an increasing cation charge. Since the difference in affinity for HFC-125 and CO₂ is not drastic with zeolite 5A (see Figure S17), it is reasonable to think that the smaller diffusion coefficient for HFC-125 primarily is a result of increased steric hinderances during diffusion.

A comparison of the activation energy for diffusion between CO_2 and HFC-125 in zeolite 5A agrees with the relative magnitudes of the time constants and diffusion coefficients in Table 5. Garcés-Polo et al.⁴² reported an average E_A of 21.4 kJ/mol for CO_2 and zeolite 5A below 0.1 MPa, whereas Kamiuto et al.⁵³ reported 29.7 kJ/mol for the same system. The activation energy for HFC-125 in zeolite 5A at $1.25 \cdot 10^{-2}$ MPa and $2.50 \cdot 10^{-2}$ MPa was 43.48 kJ/mol and 35.50 kJ/mol, respectively, as shown in Table 5.

It is interesting to note that kinetic data greater than 3.75·10⁻² MPa at 298.15 K and greater than 2.50·10⁻² MPa at both 323.15 K and 348.15 K indicates a faster diffusion rate for HFC-125 in zeolite 5A. As a result, time constants could not be obtained from kinetic data measured at higher pressures since Equation 42 could not be fit. Optimization of the experimental conditions, such as pressure ramp rate, may allow gravimetric data to be obtained and fitted, in order to calculate time constants at higher pressures. However, there are limitations to the use of the gravimetric technique to measure the kinetics of fast adsorption processes. The rate of pressurization is generally controlled at a rate slow enough to prevent disturbance of the balance reading, but this means the kinetics of fast adsorption processes cannot be studied under isothermal conditions. Conversely, pressure cannot be increased too quickly, otherwise the balance reading will be disturbed by gas flow, rather than accurately reflecting the rate of adsorption. Furthermore, at the highest pressures, the amount of adsorption between pressure points is relatively small, due to the Type I behavior exhibited by both HFC-32 and HFC-125 on zeolite 5A, and so the gravimetric signal will be too small to extract meaningful kinetic information. Nevertheless, if enough external energy is supplied, it is possible that at pressures and temperatures above the aforementioned conditions,

HFC-125 could overcome the activation energy for diffusion resulting from both steric hinderances and strong adsorbate-adsorbent interactions.

The increase in diffusion rate at higher pressures is consistent with results from our previous study. ¹⁸ It was observed that adsorption capacity of HFC-32 increased in zeolite 4A as the temperature increased, and this was attributed to a slight increase of effective pore diameter with the increasing temperatures. It is possible that the same phenomenon occurred with zeolite 5A, which in turn led to a faster diffusion rate of HFC-125 through the structure. It is also reasonable to think that the activation energy for diffusion decreases at higher pressures and temperatures, which would also lead to an increased rate of diffusion. Note that the activation energy for diffusion decreased by almost 8 kJ/mol with an increase in pressure of only 1.25·10⁻² MPa. It is expected that the activation energy for diffusion will continue to decrease with an increase in pressure.

The diffusion of HFC-32 into zeolite 5A was too fast to accurately model using Equation 33 and similar results were observed with HFC-125 for pressures in the range of $3.75 \cdot 10^{-2}$ MPa to 1.0 MPa. The separation of R-410A using zeolite 5A would be designed based on the thermodynamic state of the system at a given temperature, pressure, and composition. This is in contrast to a separation based on the difference in rates of diffusion of the adsorbing species. HFC-125 would encounter more steric hinderances than HFC-32 while diffusing into the zeolite; however, no substantial diffusion limitations were observed using gravimetric measurements.

Conclusion

Binary adsorption of HFC-125 and HFC-32 was measured using both Hiden Isochema IGA and XEMIS gravimetric microbalances with the IMB method (IGA+IMB and XEMIS+IMB), and measurements were consistent with pure gas adsorption results measured in our previous study using a XEMIS microbalance. Zeolite 5A has a preferential adsorption for HFC-32 over HFC-125 over most of the gas phase composition range and is an excellent candidate for the separation of R-410A with a selectivity of approximately 9.7.

IAST was used with three different pure gas isotherm models (DSL, Tóth, and Jensen and Seaton) to predict binary adsorption of HFC-32 and HFC-125 on zeolite 5A. The IAST-DSL model

provided the most accurate predictions. All IAST models provided good qualitative accuracy when compared to experimental data. Good quantitative predictions for adsorbed phase mole fractions were made for HFC-32 but not for HFC-125. The poor quantitative predictions for HFC-125 were attributed to adsorbed phase nonidealities associated with competitive adsorption of HFC-32 over HFC-125. HFC-32 preferentially filled high-energy adsorption sites during coadsorption. HFC-32 molecules behave similar to pure gas adsorption but this was not the case for HFC-125. Competitive adsorption behavior was attributed to more favorable enthalpic and entropic interactions between HFC-32 and zeolite 5A compared with those for HFC-125.

The nonideal adsorption behavior of HFC-125 was validated through activity coefficients, which were less than unity for HFC-125 compared with HFC-32 values closer to one. Fitting parameters for the activity coefficient models supported the hypothesis of molecular-level competitive adsorption behavior between HFC-125 and HFC-32. The experimental activity coefficients were used in RAST, and three separate RAST models were investigated: RAST-SPD, RAST-N, and RAST-W. RAST-N provided the highest accuracy for predicting binary adsorption behavior of HFC-32 and HFC-125 with zeolite 5A. Using the RAST-N model greatly improved selectivity trends compared with IAST-DSL predictions. Both qualitative and quantative accuracy is important for developing a binary adsorption model.

Kinetic data from pure gas adsorption measurements for HFC-125 and HFC-32 with zeolite 5A provided further insight into the separation process. HFC-125 diffusion coefficients could be calculated by fitting the kinetic data to the isothermal Fickian diffusion model for a spherical particle at pressure less than $3.75 \cdot 10^{-2}$ MPa and were in the range of $7.73 \cdot 10^{-17}$ to $1.68 \cdot 10^{-16}$ m²/s. For practical separation of R-410A using zeolite 5A, it is expected based on gravimetric results that diffusion limitations will not be a significant issue.

Associated Content

Supporting Information: Derivations of thermodynamic and kinetic models, modified activity coefficient models, adsorbed phase activity coefficient calculation methods, XEMIS+IMB binary adsorption data, additional graphs for adsorption results and model fits, kinetic data from gravimetric measurements, and Arrhenius plots.

Acknowledgements

The authors would like to thank Hiden Isochema engineers Daniel Stirrup, Matthew Gee, and Luke Wilkinson for technical support with the XEMIS+IMB. The authors would also like to thank Dr. Orhan Talu for providing guidance with calculating experimental adsorbed phase activity coefficients. This material is based upon the work supported by the National Science Foundation under grant no. 2029354.

References

- Masson-Delmotte, V.; Zhai, P.; A. Pirani, S.; Connors, L.; Péan, C.; Berger, S.; Caud, N.; Chen, Y.; Goldfarb, L.; Gomis, M. I.; Huang, M.; Leitzell, K.; E. Lonnoy; Matthews, J. B. R.; Maycock, T. K.; Waterfield, T.; Yelekçi, O.; Yu, R.; Zhou, B. *Climate Change 2021: The Physical Science Basis*; IPCC AR6 WGI; Intergovernmental Panel on Climate Change: Cambridge, IL, Aug. 7, 2021, 2021.
- (2) Yancey, A. D.; Terian, S. J.; Shaw, B. J.; Bish, T. M.; Corbin, D. R.; Shiflett, M. B. A Review of Fluorocarbon Sorption on Porous Materials. *Micropor. Mesopor. Mat.* **2022**, *331*, 111654.
- (3) Booten, C.; Nicholson, S.; Mann, M.; Abdelaziz, O. *Refrigerants: Market Trends and Supply Chain Assessment*; NREL/TP-5500-70207; Clean Energy Manufacturing Analysis Center: Golden, CO, 2020.
- (4) Clemmer, P. G.; Tung, H. S.; Smith, A. M. Process for the Purification of a Pentafluoroethane Azeotrope. U.S. Patent 5,346,595, Sep. 13, 1994.
- (5) Mahler, B.; Miller, R. Process for Separating Pentafluoroethane from a Mixture Comprising Halogenated Hydrocarbons and Chloropentafluoroethane. WO95/21147, Aug. 10, 1995.
- (6) Miller, R. N. Extractive Distillation Process for Separating Difluoromethane and Pentafluoroethane Using Methylene Chloride. U.S. Patent 6,156,161, Dec. 5, 2000.
- (7) Motkuri, R. K.; Annapureddy, H. V.; Vijaykumar, M.; Schaef, H. T.; Martin, P. F.; McGrail, B. P.; Dang, L. X.; Krishna, R.; Thallapally, P. K. Fluorocarbon adsorption in hierarchical porous frameworks. *Nat. Commun.* **2014**, *5*, 4368.
- (8) Peng, Y.; Zhang, F.; Zheng, X.; Wang, H.; Xi, C.; Xiao, Q.; Zhong, Y.; Zhu, W. Comparison Study on the Adsorption of CFC-115 and HFC-125 on Activated Carbon and Silicalite-1. *Ind. Eng. Chem. Res.* **2010**, *49* (20), 10009-10015.
- (9) Sosa, J. E.; Malheiro, C.; Ribeiro, R. P. P. L.; Castro, P. J.; Piñeiro, M. M.; Araújo, J. M. M.; Plantier, F.; Mota, J. P. B.; Pereiro, A. B. Adsorption of fluorinated greenhouse gases on activated carbons: evaluation of their potential for gas separation. *J. Chem. Technol. Biot.* **2020**, *95* (7), 1892-1905.
- (10) Stephenson, N. C.; Walker, B. B.; Spencer, C. W. Refrigerant Separation. WO 96/30109, Oct. 3 1996, 1996.
- (11) Urano, K.; Iwa, Y.; Kashiwagi, D. Component separation method of mixed refrigerant and component separation device. JP 2016-073972A, May 12, 2016, 2015.

- (12) Wanigarathna, D.; Gao, J.; Liu, B. Fluorocarbon Separation in a Thermally Robust Zirconium Carboxylate Metal-Organic Framework. *Chem. Asian. J.* **2018**, *13* (8), 977-981
- (13) Wanigarathna, D.; Jiajian, G.; Liu, B. Adsorption Separation of R134a, R125 and R143a Fluorocarbon Mixtures Using 13X and Surface Modified 5A Zeolites. *AIChE J.* **2017**, *64* (2), 640-648.
- (14) Corbin, D. R.; Diebold, M. P.; Mahler, B. A. Separation of Chloropentafluoroethane from Pentafluoroethane. U.S. 5,585,529, Dec. 17, 1996, 1996.
- (15) Corbin, D. R.; Mahler, B. A. Separation of Tetrafluoroethane Isomers. U.S. 5,600,040, 1997.
- (16) Wanigarathna, D. K. J. A.; Gao, J.; Liu, B. Metal organic frameworks for adsorption-based separation of fluorocompounds: a review. *Mater. Adv.* **2020**, *1* (3), 310-320.
- (17) Wanigarathna, D.; Jiajian, G.; Takanami, T.; Zhang, Q.; Liu, B. Adsorption Separation of R-22, R-32 and R-125 Fluorocarbons using 4A Molecular Sieve Zeolite. *ChemistrySelect* **2016**, *I* (13), 3718-3722.
- (18) Yancey, A. D.; Corbin, D. R.; Shiflett, M. B. Difluoromethane (HFC-32) and Pentafluoroethane (HFC-125) Sorption on Linde Type A (LTA) Zeolites for the Separation of Azeotropic Hydrofluorocarbon Refrigerant Mixtures. *Langmuir* **2022**, *38* (6), 1937–1953.
- (19) Broom, D. P.; Talu, O.; Benham, M. J. Integral Mass Balance (IMB) Method for Measuring Multicomponent Gas Adsorption Equilibria in Nanoporous Materials. *Industrial & Engineering Chemistry Research* **2020**, *59* (46), 20478-20491.
- (20) Toth, J. State Equations of the Solid-Gas Interface Layers. *Acta. Chem. Acad. Hung.* **1971,** *69* (3), 311-328.
- Jensen, C. R. C.; Seaton, N. A. An Isotherm Equation for Adsorption to High Pressures in Microporous Adsorbents. *Langmuir* **1996**, *12* (11), 2866-2867.
- (22) Myers, A. L.; Prausnitz, J. M. Thermodynamics of Mixed-Gas Adsorption. *AICHE J.* **1965**, *11* (1), 121-127.
- (23) Simon, C. M.; Smit, B.; Haranczyk, M. pyIAST: Ideal adsorbed solution theory (IAST) Python package. *Computer Physics Communications* **2016**, *200*, 364-380.
- (24) Talu, O.; Li, J.; Myers, A. L. Activity coefficients of adsorbed mixtures. *Adsorption* **1995**, *I* (2), 103-112.
- (25) Valenzuela, D. P.; Myers, A. L.; Talu; Zwiebel, I. Adsorption of Gas Mixtures: Effect of Energetic Heterogeneity. **1988**, *34* (3), 397-402.
- (26) Cochran, T. W.; Kabel, R. L.; Danner, R. P. The Vacancy Solution Model of Adsorption-Improvements and Recommendat ions. *AICHE J.* **1985**, *31* (12), 2075-2081.
- (27) Suwanayuen, S.; Danner, R. P. Vacancy Solution Theory of Adsorption From Gas Mixtures. *AICHE J.* **1980**, *26* (1), 76-83.
- (28) Cochran, T. W.; Kabel, R. L.; Danner, R. P. Vacancy Solution Theory of Adsorption Using Flory-Huggins Activity Coefficient Equations. *AICHE J.* **1985**, *31* (2), 268-277.
- (29) Zhou, C.; Hall, F.; Gasem, K. A. M.; Robert L. Robinson, J. Predicting Gas Adsorption Using Two-Dimensional Equations of State. *Ind. Eng. Chem. Res.* **1994**, *33* (5), 1280-1289.
- (30) Siperstein, F. R.; Myers, A. L. Mixed-Gas Adsorption. *AICHE J.* **2001**, *47* (5), 1141-1159.

- (31) Dunne, J.; Myers, A. L. Adsorption of Gas Mixtures in Micropores: Effect of Differences in Size of Adsorbate Molecules. *Chem. Eng. Sci.* **1994**, *49* (17), 2941-2951.
- (32) Myers, A. L. Prediction of Adsorption of Nonideal Mixtures in Nanoporous Materials. *Adsorption* **2005**, *11*, 37-42.
- (33) Myers, A. L. Activity Coefficients of Mixtures Adsorbed on Heterogeneous Surfaces. *AICHE J.* **1983**, *29* (4), 691-693.
- (34) Talu, O.; Zwiebel, I. Multicomponent Adsorption Equilibria of Nonideal Mixtures. *AICHE J.* **1986**, *32* (8), 1263-1276.
- (35) Talu, O. Needs, status, techniques and problems with binary gas adsorption experiments. *Adv. Colloid. Interfac.* **1998,** *76-77*, 227-269.
- (36) Talu, O. Thermodynamics of Multicomponent Gas Adsorption Equilibria of Non-Ideal Mixtures. Arizona State University 1984.
- (37) Costa, E.; Sotelo, J. L.; Calleja, G.; Marron, C. Adsorption Of Binary And Ternary Hydrocarbon Gas Mixtures On Activated Corbon: Experimental Determination And Theoretical Prediction Of The Ternary Equilibrium Data. *AICHE J.* **1981**, *27* (1), 5-12.
- (38) Kaur, H.; Tun, H.; Sees, M.; Chen, C.-C. Local composition activity coefficient model for mixed-gas adsorption equilibria. *Adsorption* **2018**, *25*, 951–964.
- (39) Valenzuela, D. P.; Myers, A. L., *Adsorption Equilibrium Data Handbook*. Prentice Hall: Englewood Cliffs, New Jersey, 1989.
- (40) Luberti, M.; Mennitto, R.; Brandani, S.; Santori, G.; Sarkisov, L. Activity coefficient models for accurate prediction of adsorption azeotropes. *Adsorption* **2021**, *27*, 1191-1206.
- (41) Crank, J., *The Mathematics of Diffusion*. 2nd ed.; J. W. Arrowsmith Ltd.: Bristol, England, 1975.
- (42) Garcés-Polo, S. I.; Villarroel-Rocha, J.; Sapag, K.; Korili, S. A.; Gil, A. A comparative study of CO₂ diffusion from adsorption kinetic measurements on microporous materials at low pressures and temperatures. *Chemical Engineering Journal* **2016**, *302*, 278-286.
- (43) Karge, H. G.; Weitkamp, J., Adsorption and Diffusion. Springer: Berlin, Germany, 2008.
- (44) Ruthven, D. M. Diffusion in type A zeolites: New insights from old data. *Microporous and Mesoporous Materials* **2012**, *162*, 69-79.
- (45) Baca, K. R.; Broom, D. P.; Roper, M. G.; Benham, M. J.; Shiflett, M. B. First Measurements for the Simultaneous Sorption of Difluoromethane and Pentafluoroethane Mixtures in Ionic liquids Using the Integral Mass Balance Method. *Industrial & Engineering Chemistry Research* **2022**, *61* (27), 9774-9784.
- (46) Mortier, W. J. Zeolite Electronegativity Related to Physicochemical Properties. *J. Catal.* **1978**, *55*, 138-148.
- (47) Fu, Q.; Qin, Y.; Zhang, D.; Han, Y. Competitive Adsorption Mechanism Study of CHClF₂ and CHF₃ in FAU Zeolite. *ACS Sustain. Chem. Eng.* **2018**, *6* (8), 9804-9812.
- (48) Wu, C.-W.; Sircar, S. Comments on binary and ternary gas adsorption selectivity. *Separation and Purification Technology* **2016**, *170*, 453-461.
- (49) Krishna, R.; van Baten, J. M. Using Molecular Simulations for Elucidation of Thermodynamic Nonidealities in Adsorption of CO2-Containing Mixtures in NaX Zeolite. *ACS Omega* **2020**, *5* (32), 20535-20542.
- (50) Sandler, S. L., *Chemical, Biochemical, and Engineering Thermodynamics*. 5th ed.; John Wiley & Sons, Inc.: 2016.

- (51) Sargent, R. W. H.; Whitford, C. J., Diffusion of Carbon Dioxide in Type 5A Molecular Sieve. In *Molecular Sieve Zeolites-II*, Flanigen, E. M.; Sand, L. B., Eds. American Chemical Society: 1971; Vol. 102, p 155163.
- (52) Perez-Carbajo, J.; Dubbeldam, D.; Calero, S.; Merkling, P. J. Diffusion Patterns in Zeolite MFI: The Cation Effect. *The Journal of Physical Chemistry C* **2018**, *122* (51), 29274-29284.
- (53) Kamiuto, K.; Goubaru, A.; Ermalina Diffusion Coefficients of Carbon Dioxide within Type 13x Zeolite Particles. *Chemical Engineering Communications* **2006**, *193* (5), 628-638.

For Table of Contents Only

